J. Fluid Mech. (1989), *vol.* 199, *pp.* 403–440
Printed in Great Britain

Numerical simulation of boundary-layer transition and transition control

By E. LAURIEN AND L. KLEISER
DFVLR, Institute for Theoretical Fluid Mechanics, Bunsenstrasse 10, D-3400 Göttingen, FRG

(Received 28 August 1987 and in revised form 4 July 1988)

The laminar–turbulent transition process in a parallel boundary-layer with Blasius profile is simulated by numerical integration of the three-dimensional incompressible Navier–Stokes equations using a spectral method. The model of spatially periodic disturbances developing in time is used. Both the classical Klebanoff-type and the subharmonic type of transition are simulated. Maps of the three-dimensional velocity and vorticity fields and visualizations by integrated fluid markers are obtained. The numerical results are compared with experimental measurements and flow visualizations by other authors. Good qualitative and quantitative agreement is found at corresponding stages of development up to the one-spike stage. After the appearance of two-dimensional Tollmien–Schlichting waves of sufficiently large amplitude an increasing three-dimensionality is observed. In particular, a peak–valley structure of the velocity fluctuations, mean longitudinal vortices and sharp spike-like instantaneous velocity signals are formed. The flow field is dominated by a three-dimensional horseshoe vortex system connected with free high-shear layers. Visualizations by time-lines show the formation of Λ-structures. Our numerical results connect various observations obtained with different experimental techniques. The initial three-dimensional steps of the transition process are consistent with the linear theory of secondary instability. In the later stages nonlinear interactions of the disturbance modes and the production of higher harmonics are essential.

We also study the control of transition by local two-dimensional suction and blowing at the wall. It is shown that transition can be delayed or accelerated by superposing disturbances which are out of phase or in phase with oncoming Tollmien–Schlichting instability waves, respectively. Control is only effective if applied at an early, two-dimensional stage of transition. Mean longitudinal vortices remain even after successful control of the fluctuations.

1. Introduction

The process of laminar–turbulent transition in boundary layers has been the subject of many experimental and theoretical studies. Transition under 'natural' conditions is influenced by a variety of factors, and different routes to turbulence have been discovered. Great progress has been made in the investigation of the classical problem of 'ribbon-induced' transition in the Blasius boundary layer, which is also considered in the present work. Here the transition process is initiated by monoharmonic two-dimensional instability waves, the so-called Tollmien–Schlichting waves, under carefully controlled conditions. The experiments by Klebanoff, Tidstrom & Sargent (1962), Kovasznay, Komoda & Vasudeva (1962), Hama & Nutant (1963) and Wortmann (1977) demonstrated that the onset of three-

dimensionality is an essential feature in the transition process. Williams, Fasel & Hama (1984) measured all three components of the instantaneous velocity field over a whole time-period of the process and over a wide range in the normal and spanwise direction. Their experimental results will be used for a comparison with our numerical simulations. In the following we briefly introduce some basic facts on the transition process. More detailed reviews are given by Tani (1969), Arnal (1984) and Herbert (1988). For further information on recent work we refer to the conference proceedings edited by Eppler & Fasel (1980) and Kozlov (1985).

Transition to turbulence proceeds through a sequence of regular stages. At a certain downstream distance the initially two-dimensional Tollmien–Schlichting waves develop a significant, almost periodic variation in the spanwise direction. The fluctuations grow rapidly at the spanwise so-called 'peak' positions, whereas in between at the 'valley' positions the growth occurs only further downstream. At the peak positions sharp low-velocity pulses in the instantaneous velocity signals, the so-called 'spikes', are observed. The spike signals are connected with instantaneous free high-shear layers. Simultaneously with the onset of three-dimensionality a system of mean longitudinal vortices develops. Further downstream the regular flow structures break down forming new, smaller structures. Local spots of turbulence are generated which grow as they travel downstream until a fully turbulent boundary layer is formed. From their experimental visualizations with hydrogen bubbles Hama & Nutant (1963) inferred that the high-shear layer is connected with an instantaneous three-dimensional vortex loop. In the smoke visualizations by Saric, Kozlov & Levchenko (1984) this vortex appears as a downstream-travelling Λ-shaped structure. Depending on the parameters basically two patterns of Λ-structures are observed: the classical K-type (named after Klebanoff), where the lambdas follow each other at the same spanwise position, and the subharmonic type, where subsequent spanwise rows of lambdas are shifted by half a wavelength in the spanwise direction. The subharmonic type was also investigated experimentally by Kachanov & Levchenko (1984). It may occur at smaller Tollmien–Schlichting amplitudes than the K-type. Kachanov (1987) evaluates experimental data on K-type transition from the viewpoint of the wave-resonance concept.

Theories have so far been successful only in describing the first stages of the transition process. The instability of the laminar boundary layer with respect to small disturbances is well described by the classical linear stability theory. The amplification of three-dimensional disturbances has been explained by a weakly nonlinear wave resonance (Craik 1971) and later by a linear secondary instability (Orszag & Patera 1983; Herbert 1983, 1988). According to the secondary instability theory the basic flow with superimposed finite-amplitude Tollmien–Schlichting waves becomes unstable with respect to small three-dimensional disturbances. Both the K-type and the subharmonic type are described. At given parameters a band of spanwise wavelengths may be amplified, the amplification rate being strongly dependent on the two-dimensional wave amplitude.

Transition to turbulence in the Blasius boundary layer has also been investigated by numerical simulations, solving directly the three-dimensional time-dependent Navier–Stokes equations (Orszag & Patera 1983 and Wray & Hussaini 1984 for the K-type, Spalart & Yang 1987 for the subharmonic and the mixed type). Good agreement with experiments has been obtained even in the stages of nonlinear development up to the spike stage (Wray & Hussaini 1984). In plane Poiseuille flow, where very similar phenomena are observed, simulations have been reported among

others by Orszag & Kells (1980), Orszag & Patera (1981, 1983), Zang & Hussaini (1985*a*) and the present group (Kleiser 1982; Kleiser & Schumann 1984; Kleiser & Laurien 1985*a*). A review of numerical simulations of transition is given by Zang & Hussaini (1987).

In the present paper we report numerical simulations of the transition process in a model of the Blasius boundary layer (cf. Laurien 1986; Laurien & Kleiser 1986). The model of timewise developing, spatially periodic disturbances in streamwise and spanwise directions is used. The numerical results are compared in detail with experimental data by other authors. The aim of this study is a further documentation and a better understanding of the three-dimensional stages of the transition process. As an application of our method, the interactive control of the transition process by wave superposition is simulated.

Control of the transition process is of considerable technical interest. Turbulent boundary layers have a much higher wall-shear stress and heat flux compared to laminar flows. Thus a delay of transition may reduce the drag on slender rigid bodies. Triggering of transition, on the other hand, is needed in wind-tunnel testing to simulate a higher Reynolds number flow in a given facility. Well-established boundary-layer control techniques are based on a stabilization of the mean laminar boundary-layer profile. These techniques include profile design with suitable pressure gradients, continuous wall suction and wall cooling (in air). A more recent boundary-layer control technique is based on a direct control of the instability waves. Here controlled disturbances are locally superposed on the disturbances already present in the flow in order to reduce their amplitude. This control technique has been referred to as 'active' (or 'interactive'). Experimental investigations have demonstrated that a delay or a triggering of Tollmien–Schlichting waves (Milling 1981; Liepmann, Brown & Nosenchuck 1982) and even a delay of breakdown to turbulence (Liepmann & Nosenchuck 1982; Thomas 1983; Strykowski & Sreenivasan 1985) is possible. In these experiments two-dimensional periodic disturbances are locally introduced downstream of a first wave generator by a second wave generator. The second wave generator is driven with the same frequency as the first and with a suitable phase shift and amplitude either to damp or to amplify the oncoming waves. Also feedback-loop control has been attempted. Experimental visualizations and hot-wire measurements of the controlled boundary layer (Thomas 1983) indicate that the disturbances remaining in the flow after control are different from linear waves. The flow appears to be three-dimensional downstream of the second wave generator even if transition has been delayed.

Theoretical work on active control of transition by wave superposition is rather scarce. Metcalfe *et al.* (1986) studied the control of two-dimensional Tollmien–Schlichting waves by periodic wall forcing. The behaviour of three-dimensional finite-amplitude disturbances has only been studied in boundary layers with steady wall heating (Zang & Hussaini 1985*b*). In §6 of the present study we investigate the effect of a control by two-dimensional periodic suction/blowing at the wall on the two- and three-dimensional disturbances already present in the flow. No attempt has been made to simulate a control experiment quantitatively, but potential and limitations of interactive transition control are illuminated. A corresponding investigation in Poiseuille flow has been undertaken by Kleiser & Laurien (1985*b*).

2. Mathematical model

In our numerical investigations we use a simple mathematical model of the transition process in the Blasius boundary layer. Similarly as done in classical linear stability theory, we investigate the development of disturbances in a parallel boundary layer at a fixed downstream position $\tilde{x}_1'$. The undisturbed boundary layer is defined by the Blasius profile $U_1(x_3)$ where x_3 denotes the non-dimensional wall distance. All quantities are non-dimensionalized with the free-stream velocity U_∞ and the reference length $\delta_r = (\nu \tilde{x}_1'/U_\infty)^{\frac{1}{2}}$, where ν is the kinematic viscosity. Thus the Reynolds number becomes $R = U_\infty \delta_r/\nu = (U_\infty \tilde{x}_1'/\nu)^{\frac{1}{2}}$. The boundary-layer thickness and the Reynolds number are kept fixed in our simulations, neglecting the streamwise growth. As in corresponding transition experiments, the dominant initial disturbance is a two-dimensional Tollmien–Schlichting wave. We use a coordinate system $x_1 = x_1' - c_{TS} t$ moving downstream with the phase velocity c_{TS} of that wave (figure 1). Because of Galileian invariance this is equivalent to a calculation in the rest frame, but it does reduce time-differencing errors and enables one to observe the formation of transitional flow structures roughly at a fixed place within the computational box. The disturbances in our model are periodic in the streamwise (x_1) and spanwise (x_2) directions with given wavelengths L_1 and L_2. Beginning with an initial velocity distribution specified later the disturbances develop in time, whereas in transition experiments a time-periodic flow develops downstream. Accordingly, the downstream and time coordinates will be interchanged to compare our results with experimental data. For example, we define the (local) mean of the velocity component u_j by

$$\bar{u}_j = \frac{1}{L_1} \int_0^{L_1} u_j \, \mathrm{d}x_1 \quad (j = 1, 2, 3), \tag{1a}$$

and the root-mean-square (r.m.s.) fluctuation as

$$u_j' = (\overline{(u_j - \bar{u}_j)^2})^{\frac{1}{2}} \quad (j = 1, 2, 3), \tag{1b}$$

respectively. The basic equations of motion are the Navier–Stokes equations

$$\frac{\partial \boldsymbol{u}}{\partial t} = \boldsymbol{u} \times \operatorname{curl} \boldsymbol{u} - \nabla q + \frac{1}{R} \Delta \boldsymbol{u} + \boldsymbol{f}, \tag{2}$$

$$\operatorname{div} \boldsymbol{u} = 0, \tag{3}$$

where $\boldsymbol{u}$ is the velocity, q the pressure head and $\boldsymbol{f} = (f_1, 0, 0)$ a forcing term. The latter is independent of x_1 and x_2 and is introduced in order to define the *global* mean (i.e. (x_1, x_2)-averaged) velocity profile. Two options have been used for the choice of f_1. In the first, f_1 is defined formally such that it cancels the instantaneous (x_1, x_2)-averaged values of the viscous stress and the Reynolds stress (see equation (1) of Spalart & Yang 1987), i.e. the (x_1, x_2)-averaged streamwise velocity is frozen at the Blasius profile. Thus the nonlinear distortion of the global mean flow is neglected in this model. However, the local mean flow defined in (1*a*) still depends on x_2 and x_3. The results presented herein have been obtained with this model. The second option is the choice $f_1 = f_B := -(1/R)\,\mathrm{d}^2 U_1/\mathrm{d}x_3^2$, which preserves the initial Blasius profile if no disturbances are present. This option has been used in a comparison run in order to demonstrate that the neglect of the mean flow distortion does not introduce significant errors into the disturbance development in our simulations (see the discussion below and at the end of §4).

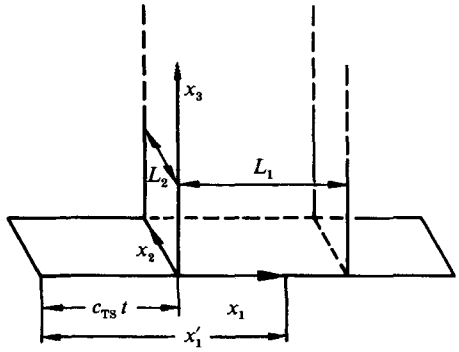

FIGURE 1. Coordinate system and integration domain.

The boundary conditions are the conditions of periodicity in the horizontal directions and

$$\boldsymbol{u}(x_1, x_2, x_3 = 0, t) = (-c_{TS}, 0, u_{3W}(x_1, t)) \tag{4}$$

$$\boldsymbol{u}(x_1, x_2, x_3 \to \infty, t) = (1 - c_{TS}, 0, 0). \tag{5}$$

In (4) u_{3W} is a prescribed normal velocity at the wall with zero mean flux which will be used to model wall suction/blowing. It is zero in uncontrolled transition. The initial velocity distribution is assumed in the form

$$\boldsymbol{u}(\boldsymbol{x}, t = 0) = \boldsymbol{U} + A_{TS}\,\boldsymbol{u}_{TS} + A_{3D}\,\boldsymbol{u}_{3D}, \tag{6}$$

consisting of the basic flow $\boldsymbol{U} = (U_1 - c_{TS}, 0, 0)$, a two-dimensional Tollmien–Schlichting wave $\boldsymbol{u}_{TS}$ with streamwise wavelength L_{TS} (wavenumber α_{TS}) and a pair of oblique waves with wavenumbers $(\alpha_1, \pm\alpha_2)$. Here $\alpha_j = 2\pi/L_j$ $(j = 1, 2)$, and $\alpha_{TS} = 2\pi/L_{TS}$. For K-type transition we use $L_1 = L_{TS}$, and for subharmonic transition $L_1 = 2L_{TS}$. The initial disturbances $\boldsymbol{u}_{TS}$ and $\boldsymbol{u}_{3D}$ are individually normalized such that at $x_2 = 0$ their streamwise components are the pure cosine functions $\cos(\alpha_{TS} x_1)$ and $\cos(\alpha_1 x_1)$ at the respective wall distance where the maximum amplitude occurs. The least damped Orr–Sommerfeld eigensolutions are always taken. All of our initial disturbances are 'spanwise-symmetric', i.e.

$$u_j(-x_2) = (-1)^{j+1} u_j(x_2). \tag{7}$$

This initial symmetry is preserved during time integration of the Navier–Stokes equations. Exploiting this symmetry reduces the computational expenses by a factor of two.

Our mathematical model of the transition process is certainly a crude one, and its relevance to the actually observed process will have to be established by comparison with experimental data. Two aspects deserve further discussion: the treatment of the mean flow, and the use of temporally growing, streamwise-periodic disturbances.

The model of downstream-periodic disturbances cannot take into account the effects of the development of the disturbance within a single wavelength. For low amplification rates this effect is certainly small and the temporal approach is well justified. When the amplification becomes larger, as in the late stages of transition, it is no longer obvious that downstream-periodic disturbances are still able to describe the real physical process. However, Herbert (1988) points out that the restriction of Gaster's (1962) transformation to small growth rates does not apply to the secondary instability. In fact, the spatially periodic model has been used with

great success in all of the numerical simulations referred to in the introduction, both for plane Poiseuille flow and for the Blasius boundary layer. In contrast to these temporal simulations, Fasel, Rist & Konzelmann (1987) investigate spatially developing disturbances in a non-parallel boundary layer using inflow/outflow boundary conditions. These simulations have been confined to the early three-dimensional stages of transition.

While most simulations of transition have used the temporal approach, the mean flow has been treated slightly differently by the various authors. Orszag & Patera (1983) and Wray & Hussaini (1984) allowed the undisturbed mean flow to develop on a diffusive timescale towards an error function profile, which has different primary stability characteristics (see Spalart & Yang 1987). A number of authors have used a forcing term as in (2) in order to make the desired undisturbed velocity profile an exact solution of the Navier–Stokes equations. Zang & Hussaini (1985, 1987) used the option $f_1 = f_B$ defined above. This option is equivalent to prescribing the basic flow $U_1(x_3)$ and to solve the complete nonlinear disturbance equations for the deviation from this basic flow. Spalart & Yang (1987) use a more refined model where a temporally growing Blasius profile is retained in a moving reference frame by a time-dependent forcing term. This allows them to follow the disturbance development over a longer streamwise distance than is intended in the present work, where, as in the experiment of Williams *et al.* (1984), the relatively short three-dimensional stage of transition up to the beginning of the spike stage is the main interest. Forcing terms in the Navier–Stokes equations that produce a desired parallel basic flow have also been used by Milinazzo & Saffman (1985) and Huerre (1987).

3. Numerical method

To solve equations (2)–(5) numerically we employ a spectral method in space and finite differences in time. The spectral discretization is based on Fourier expansions in the horizontal directions and a Chebyshev collocation matrix method (cf. Gottlieb, Hussaini & Orszag 1984) in the normal direction. Except for the treatment of the normal direction, the numerical procedures are essentially the same as described by Kleiser & Schumann (1984) and used also by a number of other investigators. The method is described in detail by Laurien (1986). Time differencing of (2) by the second-order Adams–Bashforth scheme for the nonlinear term $\boldsymbol{N} = \boldsymbol{u} \times \operatorname{curl} \boldsymbol{u} + \boldsymbol{f}$ and the Crank–Nicholson scheme for the linear terms gives

$$\Delta \boldsymbol{u}^{n+1} - \frac{2R}{\Delta t} \boldsymbol{u}^{n+1} - 2R \nabla q^{n+1} = -\boldsymbol{r}, \tag{8}$$

where $\boldsymbol{r} = 2R[\boldsymbol{u}^n/\Delta t + 1.5\boldsymbol{N}^n - 0.5\boldsymbol{N}^{n-1}] + \Delta \boldsymbol{u}^n$, $\boldsymbol{u}^n \approx \boldsymbol{u}(n\Delta t)$ etc. and Δt denotes the timestep. To decouple the components of (8) and satisfy (3) we use the Poisson equation for the pressure and the influence matrix technique to obtain the correct pressure boundary conditions (Kleiser & Schumann 1980, 1984). Equations

$$\Delta q^{n+1} = \frac{1}{2R} \operatorname{div} \boldsymbol{r}^n, \tag{9}$$

$$\operatorname{div} \boldsymbol{u}^{n+1} = 0, \quad x_3 = 0, \tag{10}$$

$$\operatorname{div} \boldsymbol{u}^{n+1} = 0, \quad x_3 \to \infty, \tag{11}$$

together with (4), (5) and (8) give a sufficient condition for (3). In the horizontal directions we expand any dependent variable, e.g. $\boldsymbol{u}$, in a Fourier series

$$\boldsymbol{u}(\boldsymbol{x},t) = \sum_{k_1}\sum_{k_2} \hat{\boldsymbol{u}}(k_1,k_2,x_3,t)\exp(\mathrm{i}k_1\alpha_1 x_1 + \mathrm{i}k_2\alpha_2 x_2), \tag{12}$$

where $|k_j| < \frac{1}{2}N_j$, $\alpha_j = 2\pi/L_j$, $j = 1,2$, $\mathrm{i} = \sqrt{-1}$. For the remainder of this section all variables $\boldsymbol{u}, q, r, u_{3\mathrm{W}}$ are understood as complex Fourier coefficients at the new time layer $n+1$. The expansion (12) is truncated outside the wavenumber range $|k_1|/N_1 + |k_2|/N_2 < \frac{2}{3}$ in order to reduce aliasing errors in the computation of nonlinear terms by the pseudospectral method. For each mode $(k_1,k_2) \neq (0,0)$ the system (4), (8)–(11) is reduced to a set of Helmholtz equations with Dirichlet boundary conditions which are solved sequentially. The numerical method described below ensures that the boundary conditions at infinity, (5) and (11), are always satisfied. Therefore only the wall pressure values are unknown and the influence matrices are reduced to scalars in the present case.

In order to apply a Chebyshev spectral method in the normal direction x_3 the semi-infinite domain $0 \leqslant x_3 < \infty$ is transformed onto the interval

$$0 < \eta \leqslant 1 \text{ by } \eta = \exp(-x_3/\gamma),$$

where γ is a free parameter (Spalart 1984). Formally the functions to be approximated are extended to the half interval $-1 \leqslant \eta \leqslant 0$ by zero. Accordingly, the computational dependent variables, which have to vanish at infinity, are chosen as the physical variables minus their value at infinity, e.g. $U_1 - 1$. In the transformed variable η we expand any function u into Chebyshev polynomials $T_k(\eta) = \cos(k\cos^{-1}\eta)$ and use collocation in the points $\eta_j = \cos(\pi j/M)$, $j = 0,\ldots,M$:

$$u(\eta_j) = \sum_{k=0}^{M} u_k T_k(\eta_j) \quad (j = 0,\ldots,M). \tag{13}$$

Typical functions of interest are of the form $u(x_3) = \exp(-bx_3)(b > 0)$, or, in the transformed variable, $u(\eta) = 0$, $-1 \leqslant \eta \leqslant 0$; $u = \eta^{b\gamma}$, $0 < \eta \leqslant 1$. In general, some higher derivatives possess a singularity at $\eta = 0$, destroying infinite-order convergence. However, if $b\gamma$ is large enough (of order 10), the coefficients decay very rapidly (e.g. by a factor of 10^{15} within $k < 50$). (More rapid convergence at smaller values of $b\gamma$ is obtained using the modified transform $x_3 = -\gamma(\ln\eta - \gamma'(\ln\eta)^2)$ with γ' of order 5 (F. Meyer, private communication, 1987)). If we choose M even, then all computational variables vanish at the collocation point $\eta = 0 (x_3 = \infty)$, and only the $N_3 = \frac{1}{2}M$ grid point values in $x_{3j} = -\gamma\ln\eta_j$, $j = 0,\ldots,N_3-1$, need to be computed and stored (calculations with M odd, $N_3 = \frac{1}{2}(M+1)$ work as well). The exponential mapping of the semi-infinite domain to the interval $[0,1]$ rather than $[-1,1]$ avoids placing too many collocation points far away from the wall. Alternative approaches are discussed in Spalart (1986) and Canuto *et al.* (1987). To calculate pth derivatives we use the matrix collocation method,

$$\frac{\mathrm{d}^p u}{\mathrm{d}\eta^p}(\eta_j) = \sum_{k=0}^{M} D_{jk}^{(p)}\, u(\eta_k) \quad (j = 0,\ldots,M), \tag{14}$$

where $\{D_{jk}^{(p)}\}$ is a matrix given e.g. by Gottlieb *et al.* (1984). In x_3-space (14) is transformed into

$$\frac{\mathrm{d}^p u}{\mathrm{d}x_3^p}(x_{3j}) = \sum_{k=0}^{N_3-1} \tilde{D}_{jk}^{(p)}\, u(x_{3k}) \quad (j = 0,\ldots,N_3-1), \tag{15}$$

using a transformed derivative matrix $\tilde{D}_{jk}^{(p)}$, where

$$\tilde{D}_{jk}^{(1)} = D_{jk}^{(1)} \frac{\partial \eta}{\partial x_3}(x_{3j}) \quad (j,k = 0,\ldots,N_3-1), \tag{16}$$

and the matrices $\{\tilde{D}_{jk}^{(p)}\}$ for $p > 1$ are calculated by applying the chain rule to the right-hand side of (16).

A straightforward application of the collocation discretization of (4), (5), (8)–(11) using the influence matrix technique leads to approximation errors in the continuity equation. These can be eliminated, at minimal computational expense, by superposition of precomputed auxiliary solutions in the same manner as the 'tau errors' arising in the tau method (Kleiser & Schumann 1980; see also the thorough discussion in the book by Canuto *et al.* 1987). The correction procedure was implemented in our code only after the present results had been obtained. However, the maximum values of div $\boldsymbol{u}$ in these transition simulations are on the order of 10^{-6} during the early stages, and the differences to the exactly divergence-free solution are insignificant. In the later spike stages the divergence-free solution is clearly superior. In addition, the correction procedure increases the stability bound on the timestep.

The method was tested first by solving the Helmholtz problem

$$u'' - b^2 u = 0, \tag{17a}$$

$$u(x_3 = 0) = 1, \quad u(x_3 \to \infty) = 0, \tag{17b}$$

with the solution $u = \exp(-bx_3)$. This serves as a model for the inhomogeneous Helmholtz problems to which the full three-dimensional problem is reduced. In the calculations the wall boundary condition is enforced, while the boundary condition at infinity is satisfied implicitly. The maximum absolute error of the solution versus N_3 is shown in figure 2 for various values of $b\gamma$. The accuracy is excellent for $b\gamma$ of order 10. For $b\gamma \gg 10$, $N_3 \approx 2(b\gamma)^{\frac{1}{2}}$ grid points are needed to resolve the boundary layer at $\eta = 1$. As there is an optimal stretching parameter γ for a given decay rate b, γ should be adapted to the actual range of decay rates b of the problem at hand to obtain optimal convergence.

As a second test we solved the Orr–Sommerfeld eigenvalue problem. The problem was formulated as an algebraic eigenvalue problem and was solved for a wide range of parameters R and α_{TS}. $\gamma = 20$ gave the best approximation within the parameter range of interest and was also used in our simulations. The rapid convergence (like exponential) of the method for the first eigenvalue $c = c_r + \mathrm{i}c_i$ with increasing number of collocation points N_3 is demonstrated in figure 3, using a point near the nose of the neutral curve ($R \approx 302, \alpha_{\mathrm{TS}} \approx 0.175$) and the reference value given by Spalart (1984). The levelling-off of the error at $\epsilon \approx 10^{-7}$ is due to the finite precision of the numerically computed Blasius profile. Higher eigenvalues of the discrete part of the spectrum are also well approximated. In addition the algebraic eigenvalue problem yields an approximation to the continuous spectrum which moves towards the exact value $c_r = 1$ with increasing N_3.

The three-dimensional computer code is implemented on a Cray-1S with the vectorized innermost loop running over the (k_1, k_2)-plane. As the left-hand sides of the discretized Helmholtz equations differ only on the diagonals an efficient solution of the $4 \times N_1 \times N_2$ real, linear, full $N_3 \times N_3$ equation systems is possible by using a matrix diagonalization which can be performed simultaneously for all wavenumbers (k_1, k_2) (Patera & Orszag 1981). Thus only $O(N_3^2)$ operations per timestep and Fourier

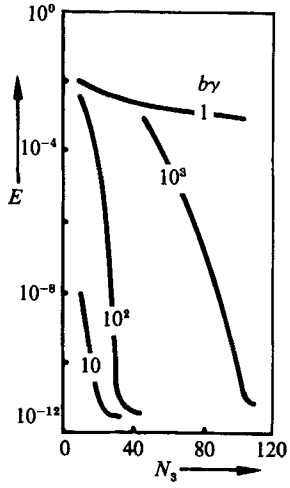

FIGURE 2. Maximum error E for the solution of the Helmholtz test problem (17) obtained with the Chebyshev collocation method for various values of $b\gamma$.

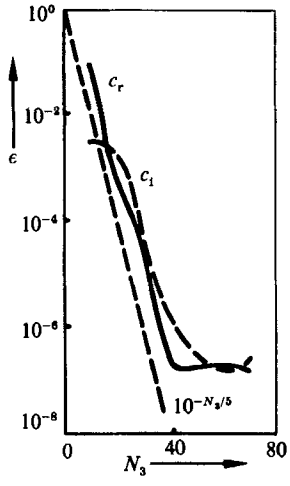

FIGURE 3. Error ϵ in least damped Orr–Sommerfeld eigenvalue $c = c_r + ic_i$ calculated with the Chebyshev collocation method *vs.* number of collocation points N_3.

mode are needed, as opposed to $O(N_3^3)$ for matrix inversion. The diagonalization is performed once in a preprocessing step. An improved version of the code which exploits the symmetry of (7) needs about 2.3 s of CPU time per timestep for a $N_1 \times N_2 \times N_3 = 32 \times 32 \times 48$ discretization.

4. Results for K-type transition

In this section the simulation results for K-type transition are documented. We compare our results to experimental investigations qualitatively and quantitatively. We choose the simulation parameters $R = 407$, $\alpha_{TS} = 0.157$ and $\alpha_2 = 0.233$, which are fitted to the experiment of Williams *et al.* (1984). We use the initial velocity distribution for the K-type according to (6). The initial disturbance amplitudes are $A_{TS} = 0.015$ and $A_{3D} = 0.001$. From the linear theory the least damped eigenvalue

$c = c_r + ic_i = 0.3727 + i0.0062$ is obtained. Thus the Tollmien–Schlichting period is $T_{TS} = 2\pi/(c_r \alpha_{TS}) = 107.4$. The numerical parameters used are $N_1 \times N_2 \times N_3 = 16 \times 16 \times 48$ and $\Delta t = 0.5$ up to $t = 1100$ and $N_1 \times N_2 \times N_3 = 32 \times 32 \times 48$, $\Delta t = 0.1$ in the time interval $1100 \leqslant t \leqslant 1340$. No numerical instability – which is well distinguishable from the physical instability – has been observed for this parameter combination.

4.1. *Development of r.m.s. fluctuations and mean flow*

The time-development of downstream-averaged quantities in the simulation corresponds to the downstream development of time-averaged experimental quantities. The timewise development of the maximum (over x_3) longitudinal r.m.s. fluctuation $u'_{1\max} = \max u'_1(x_3)$ at different spanwise positions is shown in figure 4. For $t < 750$ the flow is almost two-dimensional. Here the fluctuations grow almost exponentially. At later times the three-dimensional peak–valley splitting occurs as the fluctuations grow rapidly at $x_2 = 0$ and $x_2 = L_2$ (peaks) and less rapidly at positions in between (valleys). Figure 5 shows the distribution of u'_1 in the (x_2, x_3)-plane at three stages of development. At $t = 500$ the distribution is still almost the same as for a two-dimensional Tollmien–Schlichting wave. In the later (three-dimensional) stages the peak–valley distribution becomes visible, especially at $t = 1260$ where it is very pronounced.

In the (x_2, x_3)-plane a mean secondary flow develops along with a corresponding spanwise-periodic deformation of the mean profiles. Figure 6 shows isolines of the stream function $\psi(x_2, x_3)$ of this flow defined by $\partial\psi/\partial x_2 = \overline{u_3}, \partial\psi/\partial x_3 = -\overline{u_2}$. The streamlines indicate a pair of counter-rotating vortices with their axes in the streamwise direction. At $t = 1100$ one pair of vortices has developed. The vortices become stronger with time. At the peak position ($x_2 = 0$) slowly moving near-wall fluid is transported away from the wall, whereas at the valley position $x_2 = \frac{1}{2}L_2$ fast fluid is transported towards the wall. In the later stages a second pair of vortices develops at the valley position at a somewhat larger distance from the wall, rotating in the opposite direction to the first pair. A very similar development of the flow has been observed in experiments, e.g. by Klebanoff *et al.* (1962). An early theoretical model for the appearance of these mean longitudinal vortices has been proposed by Benney and Lin (see Benney 1964). We emphasize here that the mean flow field just considered contains only the averaged disturbance values, which at the later stages are significantly smaller than the local peaks of the instantaneous disturbances. A quantitative comparison of the mean and instantaneous vorticity field based on the present simulation data is given in Hama *et al.* (1987).

The stages of time-development in the simulation agree very well with stages of downstream development in experimental investigations. In order to compare our results quantitatively with experimental data we choose the simulated flow field at $t = 1260$ and compare with the experiments of Williams *et al.* (1984) at the station $x = 60$ cm. Figure 7 shows $u'_{1\max}$ as a function of x_2 and figure 8 shows $u'_1(x_3)$ at different spanwise positions. The quantitative agreement is considered very good if we take into account the experimental difficulties in establishing a clean, regular flow field. In particular, no control of the three-dimensional development was attempted in the experiment.

4.2. *Instantaneous flow field*

In experiments instantaneous quantities are measured at fixed spatial positions as functions of time. The corresponding quantities in our model are functions of x_1 at fixed positions x_2, x_3 and at fixed simulation times t. Figure 9 gives simulation results

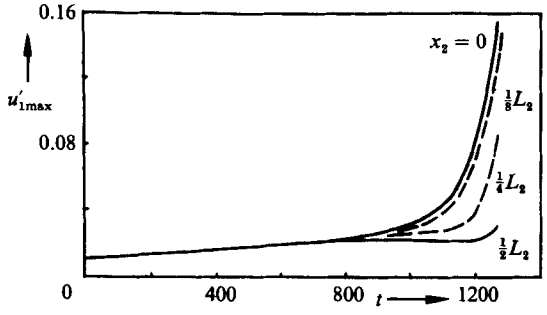

FIGURE 4. Time-development of the maximum longitudinal r.m.s. fluctuation $u'_{1\max}$ at various spanwise positions x_2.

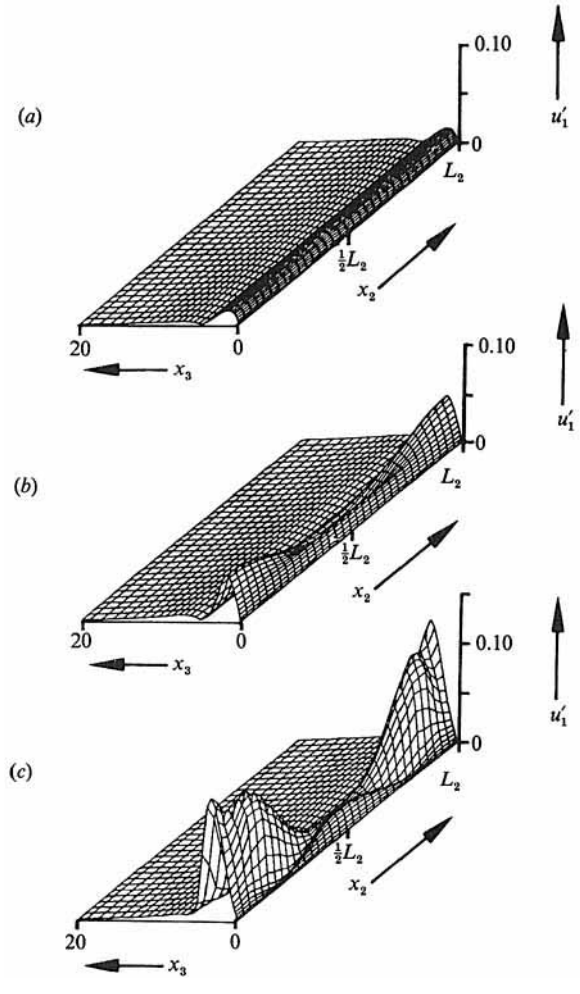

FIGURE 5. Distribution of u'_1 in the (x_2, x_3)-plane at (*a*) $t = 500$; (*b*) $t = 1150$; (*c*) $t = 1260$.

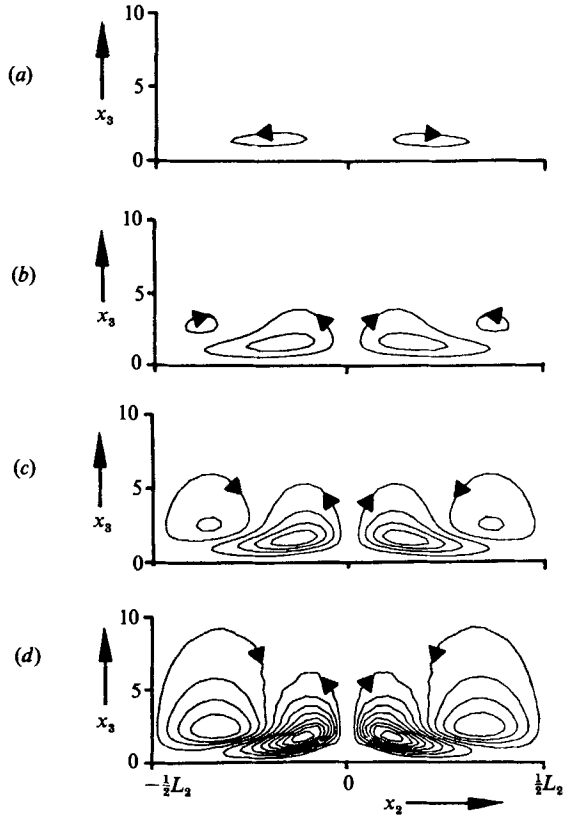

FIGURE 6. Streamlines of the mean secondary flow at (*a*) $t = 1100$; (*b*) $t = 1180$; (*c*) $t = 1220$; (*d*) $t = 1260$.

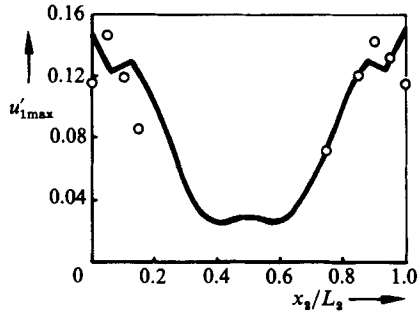

FIGURE 7. Distribution of $u'_{1\max}$ over the span. ——, simulation, $t = 1260$; ○, experiment Williams *et al.* (1984), $x = 60$ cm.

for 'time signals' of the u_1 velocity in various stages of the transition process. The initially sinusoidal signal becomes distorted in later stages and finally forms a spike-like shape.

In the following we compare the simulated flow field in the three-dimensional space at the fixed simulation time $t = 1260$ with the experimental data of Williams *et al.* (1984) in the time–space frame (i.e. the three coordinates time, spanwise and normal direction) at the fixed downstream position $x = 60$ cm. Figure 10 shows a sequence

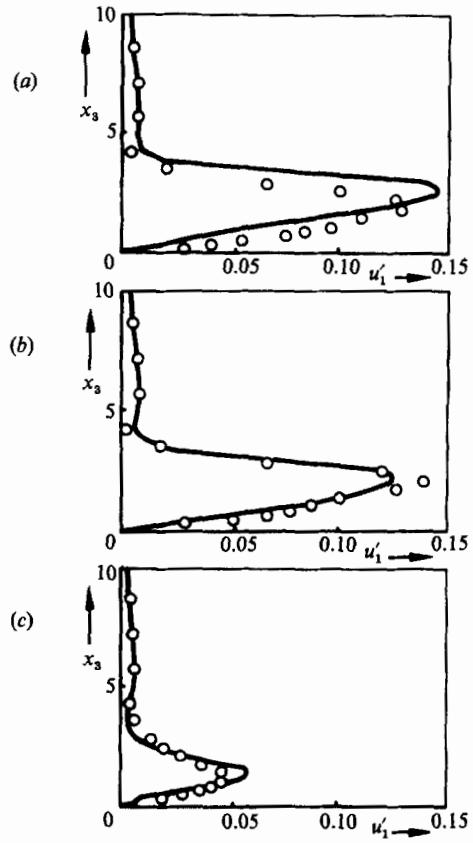

FIGURE 8. Distribution of u_1' over the normal coordinate x_3 at different spanwise positions. (*a*) $x_2/L_2 = 0$; (*b*) $x_2/L_2 = 0.0625$; (*c*) $x_2/L_2 = 0.28$. ——, simulation, $t = 1260$; ○, experiment Williams *et al.* (1984), $x = 60$ cm.

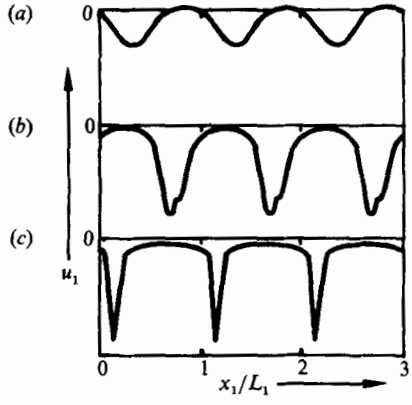

FIGURE 9. Instantaneous velocity signals at different stages of development: (*a*) $t = 1180$; (*b*) $t = 1260$; (*c*) $t = 1290$. The vertical scale is arbitrary.

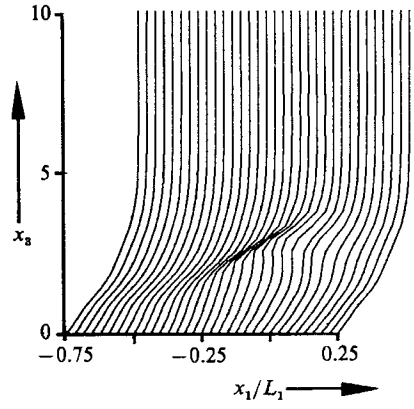

FIGURE 10. Profiles of instantaneous downstream velocity over one period at $x_2 = 0$ and $t = 1260$.

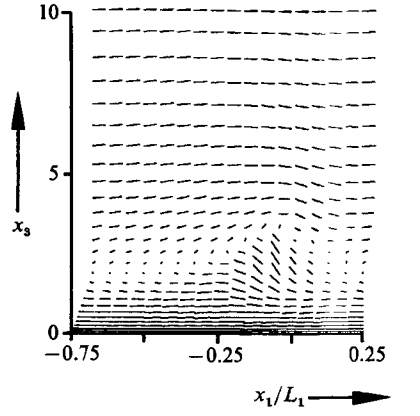

FIGURE 11. Projections of the instantaneous velocity vectors in the peak plane $x_2 = 0$ in the moving frame of reference. The starting points of the vectors are on straight vertical and horizontal lines.

of instantaneous profiles of the downstream velocity $u_1(x_1, x_3)$ in the peak plane. Each profile corresponds to a certain x_1-position of the simulation and to a certain phase position of the experiment. At some positions the profiles are strongly different from the Blasius profile. In the range $2 \leqslant x_3 \leqslant 3$ there is a region where the velocity is nearly constant over the wall distance x_3. Above this region large velocity gradients $\partial u_1/\partial x_3$ occur. This quantity is also the dominant contribution to one component of the shear stress. The simulation results are in good agreement with the experiment. Projections of the instantaneous velocity vectors in the peak position $x_2 = 0$ onto the (x_1, x_2)-plane in the moving frame of reference are plotted in figure 11. In this plane a finite-amplitude Tollmien–Schlichting wave exhibits a velocity field which contains two counter-rotating swirls with their centres, the so-called 'cat's eyes', near the critical layer $x_{3\mathrm{crit}} \approx 1$. In our diagram an instantaneous upward motion is visible in the region where the profiles in figure 10 are nearly constant. At the x_1-position of strongest upward motion we observe the largest velocity defect in the downstream component, visible as the spike signal in figure 9(*b*). In the remaining x_1-period of figure 11 there is a weak downstream velocity. Thus a swirling

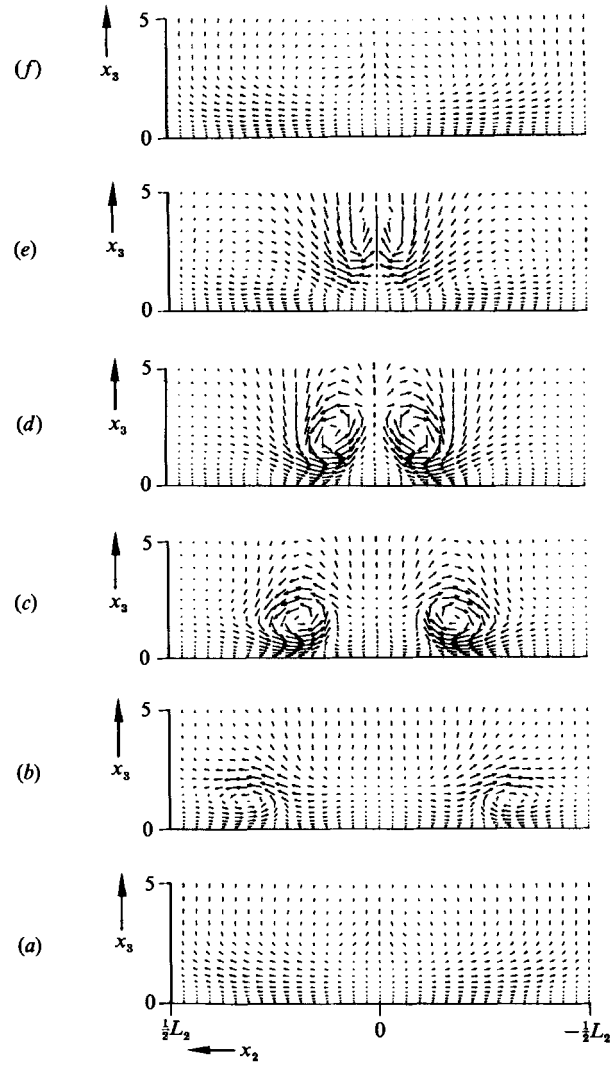

FIGURE 12. Projections of the instantaneous velocity vectors onto the planes $x_1/L_1 = j \times 0.1875$. (*a*) $j = 0$; (*b*) $j = 1$; (*c*) $j = 2$; (*d*) $j = 3$; (*e*) $j = 4$; (*f*) $j = 5$.

motion is established, which can be related to one of the cat's eyes of the original Tollmien–Schlichting wave, however strongly amplified, contracted to a small downstream region, and moved upwards.

In figure 12 we plot projections of the velocity vector at different x_1-positions onto the (x_2, x_3)-plane. A symmetric secondary swirling motion becomes visible. The centres of the swirls move towards the peak plane $x_2 = 0$ and away from the wall with increasing x_1. It becomes evident that the velocity field consists of a three-dimensional 'vortex loop' or 'horseshoe vortex'. A perspective view is given in figure 13. The centres of the swirls may be connected by a horseshoe-shaped line with its forward tip in the peak plane $x_2 = 0$ and its backward tips near the valley plane closer to the wall. This line is tilted against the horizontal plane. In the peak plane $x_2 = 0$ the horseshoe vortex induces the strong instantaneous upward motion described above near its forward tip, because here the legs of the vortex loop are very

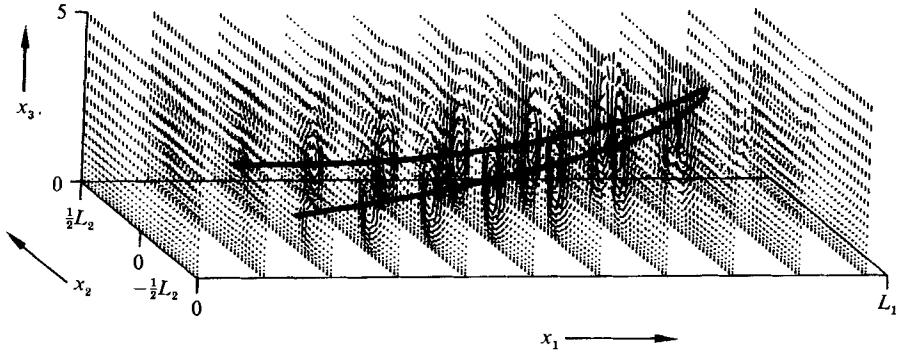

FIGURE 13. Perspective view of projections of the instantaneous velocity vectors at different x_1-positions. The centres of the swirling motions may be connected by a horseshoe-shaped line.

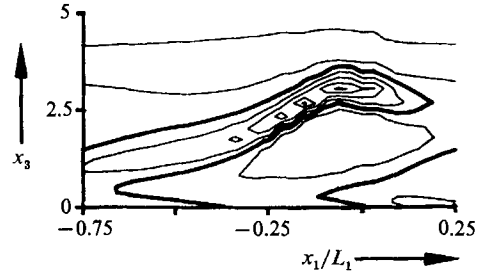

FIGURE 14. Isolines of the instantaneous spanwise vorticity at $x_2 = 0$ for $t = 1260$. The thick line corresponds to $\omega_2 = 0.29$.

close to each other. The line connecting the centres is not a vortex line (integral curve of the vorticity field). This has been checked by numerical integration of vortex lines from the computed vorticity field (see also Williams (1985) and Kleiser & Laurien (1985*a*) for a corresponding investigation in plane Poiseuille flow). Vortex lines are directed in spanwise direction over most of the spatial domain. Near the vortex loop, however, they are directed in negative or positive downstream direction due to a locally strong longitudinal vorticity component. Also, the vortex loop is not a vortex tube, i.e. surface of vortex lines which intersect a closed curve. Of course, the longitudinal mean vortex system obtained by averaging over x_1, which is shown in figure 6(*d*), is closely related to the longitudinal vorticity within the horseshoe vortex.

It is also interesting to consider the instantaneous vorticity field of the flow. The component $\omega_2 = \partial u_1/\partial x_3 - \partial u_3/\partial x_1$ is dominant. In figure 14 isolines of ω_2 in the peak position $x_2 = 0$ at $t = 1260$ are plotted. Layers of high instantaneous spanwise vorticity appear which are detached from the wall. The three-dimensional structure of the region of high spanwise vorticity is depicted in figure 15, where isolines with $\omega_2 = 0.29$ in the three-dimensional space are shown. The surface of constant vorticity has a tongue-like structure. The maximum occurs within the tip of the tongue. Subsequent tongues overlap each other. Lines of constant magnitude of the instantaneous streamwise vorticity $|\omega_1| = 0.13$ are shown in figure 16. The regions of large vorticity can be related to the legs of the horseshoe vortex shown in figure 13. The instantaneous shear $\partial u_1/\partial x_3$ is by far the dominant part of the instantaneous spanwise vorticity. For large iso-values the isoline plots of the shear $\partial u_1/\partial x_3$ are

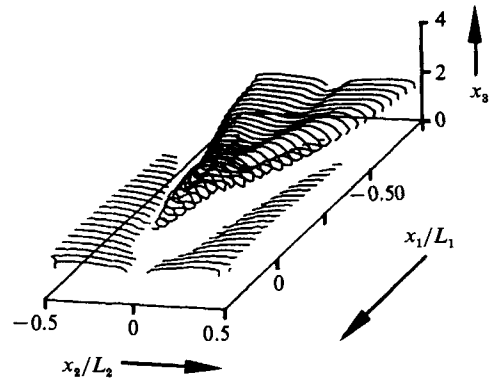

FIGURE 15. Perspective view of lines of constant instantaneous spanwise vorticity $\omega_2 = 0.29$. Lines below $x_3 = 1.1$ have been suppressed for visibility.

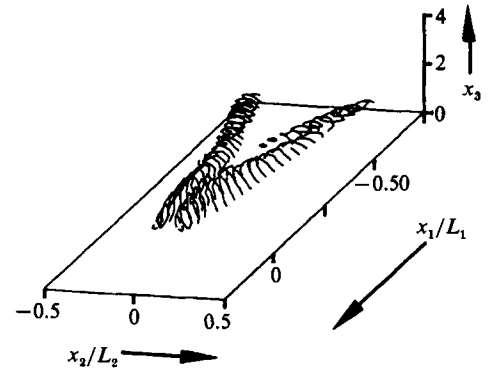

FIGURE 16. Perspective view of lines of constant instantaneous streamwise vorticity magnitude $|\omega_1| = 0.13$ (lines below $x_3 = 1.1$ are suppressed).

almost identical with ω_2 vorticity plots. In figure 17 the evolution of a constant-shear surface in the transition process is shown. Initially the surface is flat with a slight waviness in x_1-direction, which corresponds to the finite-amplitude Tollmien–Schlichting wave. In the later development the constant-shear surface folds up and forms a tongue-like structure (figure 17*b*, *c*). In the further development the tongue is stretched in downstream direction and finally forms a sharp tip.

The onset of the formation of the horseshoe vortex has been described among others by Hama & Nutant (1963). A spanwise-oriented vortex tube is considered which initially corresponds to a local maximum of the vorticity field of the Tollmien–Schlichting wave. A slight vertical waviness is amplified in the velocity field of the boundary layer, and the vortex tube is stretched and tilted. Our results show that during the stages of further development the horseshoe vortex is described by its centreline rather than by a vortex tube. Its forward tip moves upwards, whereas its backward tip moves downwards to the wall. The swirling motion around the centreline becomes stronger near the forward and weaker near the backward portion. The forward tip enters a region with higher velocity when it moves away from the wall. Thus the vortex loop is stretched in the downstream direction. The vortex tip induces locally a strong upward motion transporting a lump of slowly

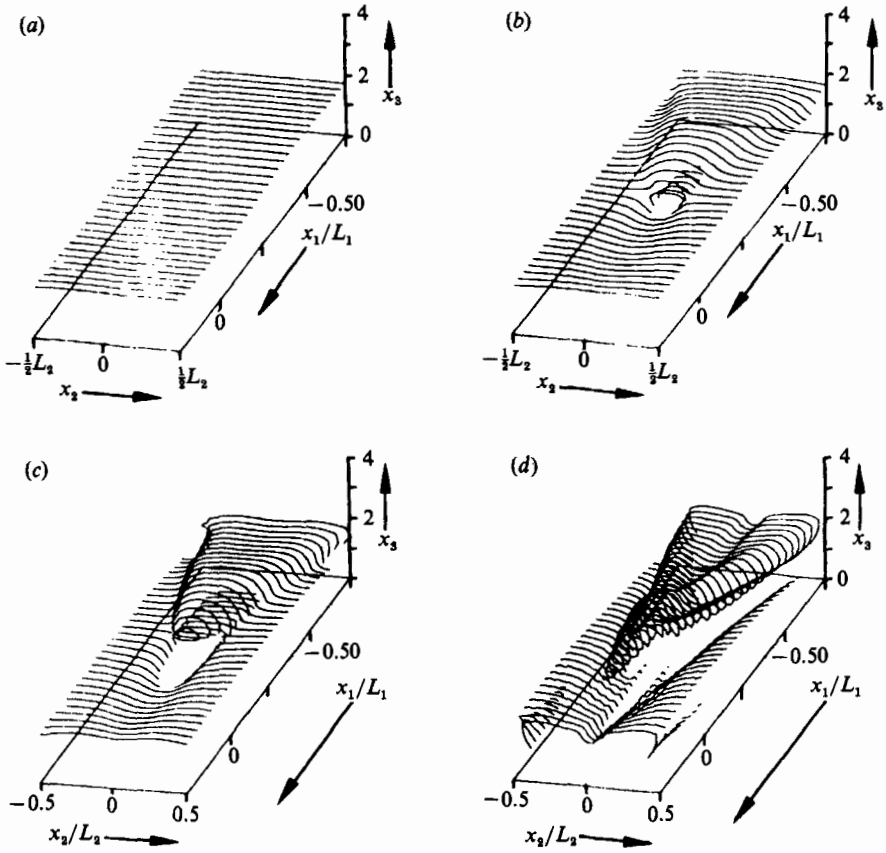

FIGURE 17. Lines of constant instantaneous shear $\partial u_1/\partial x_3 = 0.29$. (*a*) $t = 500$; (*b*) $t = 1100$; (*c*) $t = 1150$; (*d*) $t = 1260$ (lines below $x_3 = 1.1$ are suppressed).

moving fluid from the vicinity of the wall into a region of higher velocity. The oncoming faster fluid meets the slow fluid and forms a high-shear layer on top of the upward moving fluid. Very similar features of the instantaneous vorticity field have been found experimentally by Williams *et al.* (1984). We note that the agreement with these measurements is qualitatively and even quantitatively good.

4.3. *Visualization by particles*

Several important experimental investigations of boundary-layer transition use visualizations by particles. Either hydrogen bubbles, e.g. Hama & Nutant (1963); Wortmann (1977), or smoke, e.g. Saric *et al.* (1984), are introduced into the flow. We simulate such visualizations in the computed velocity field at a fixed simulation time t. We introduce a new timescale τ, relevant for the particle motion. Let $\xi(\tau)$ be the position of a particle in the rest frame, ξ_0 the initial position of the particle and $v(x', t)$ denote the velocity field in the rest frame. Then the simulated particle motion is given by

$$\frac{\partial \xi}{\partial \tau} = v(\xi_1 - c_{\mathrm{TS}}\tau, \xi_2, \xi_3; t) \quad (\xi(0) = \xi_0). \tag{18}$$

The particles move passively with the flow. While in experimental visualizations the particles move continuously into a region where the transition process is more

advanced, in our simulation the velocity field is frozen at a certain stage of development. Thus it is only the integration effect (Hama 1962) which is responsible for the formation of particle structures in our visualizations. A row of particles is started simultaneously along a straight line. This corresponds to hydrogen bubbles started at a fixed wire which is pulsed by an electrical current. This line of particles is called a *time line*. A number of rows is started within one period T_{TS}, and this process is repeated periodically. We define the phase position of a 'snapshot' as $\phi = 2\pi\tau/T_{\mathrm{TS}}$.

First we simulate visualizations with a bubble wire normal to the wall at the peak position. Fifteen time lines per Tollmien–Schlichting period, consisting of 100 particles in the x_3-direction each, are started in the velocity field at $t = 1260$. Figure 18 shows the result at three phase positions. The time lines are strongly distorted. A region with almost no particles moves downstream with the wave velocity. This region is formed shortly downstream of the wire, when the lump of slowly moving fluid described above passes. Above this region very strong distortion of some time lines indicates the position of the high-shear layer. Near the wall the structure of distinct lines disappears because the particles of an individual line have moved far away from each other.

Figure 19 shows a plan view of visualizations with a spanwise wire at $t = 1100$, i.e. in a stage of beginning three-dimensional development. Again the flow comes from the left. The wire is located at the wall distance of the critical layer $x_{3\,\mathrm{crit}} \approx 1$, where $U_1(x_{3\,\mathrm{crit}}) = c_{\mathrm{TS}}$. Per Tollmien–Schlichting period 30 time lines consisting of 100 particles each are started. The figure shows pronounced spanwise stripes. These are caused by the roll-up of the particle sheet as the side view (figure 20) shows. The stripes have a slight waviness in the spanwise direction caused by the emerging three-dimensional disturbances. The corresponding plan views are shown at $t = 1200$ (developed three-dimensional stage) in figure 21 and at $t = 1260$ (spike stage) in figure 22. In both figures 'Λ-vortices' similar to those observed in experimental visualizations are visible. The structure consists of a folded particle sheet. However, here the three-dimensional disturbances are much larger (for a discussion of the magnitude of the two- and three-dimensional disturbances see the next section). The impression of a screw-like structure of the Λ-legs is caused by the overlapping of the folded particle lines. At $t = 1260$ the line structure in the right-hand portion of figure 22 has almost disappeared. Particles have been moved far apart from each other and are merged in a seemingly unordered fashion. The instantaneous upward motion becomes visible in the side view (figure 23). A cluster of particles is swept upward into a higher velocity region where it overtakes the rest of the particles started at the same time. Our simulations of particle visualizations agree very well with those of the experiments referred to earlier.

4.4. *Behaviour of Fourier modes*

In this section we discuss the boundary-layer transition process from another point of view. The Fourier expansion of our numerical method is used to interpret the importance of the various disturbance waves contained in our model. As a measure of the magnitude of each wave the maximum (over x_3) amplitude of the Fourier coefficients of the longitudinal velocity $|\hat{u}_1(k_1, k_2)|_{\max}$ is considered. The disturbance parts are distinguished as non-fluctuating ($k_1 = 0$) or fluctuating ($k_1 \neq 0$), and as two-dimensional ($k_2 = 0$) or three-dimensional ($k_2 \neq 0$). Non-fluctuating quantities correspond to mean (i.e. x_1-averaged) quantities by definition. Because of the symmetries it is sufficient to consider the modes with $k_1 \geqslant 0$ and $k_2 \geqslant 0$ only. We have

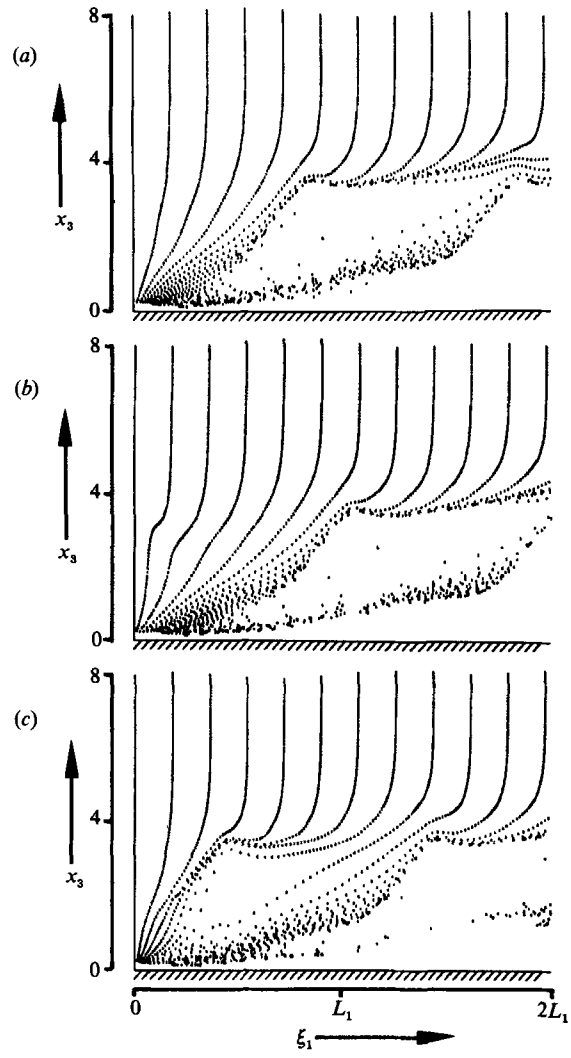

FIGURE 18. Time lines starting from a wire in the peak position (side view) at $t = 1260$. Relative phase positions are (a) $\phi = 0°$; (b) $\phi = 120°$; (c) $\phi = 240°$.

multiplied them with factors of 2 ($k_1 = 0$ or $k_2 = 0$) or 4 ($k_1 > 0, k_2 > 0$) to account for the various symmetries.

The temporal development of the amplitudes of the downstream velocity modes is plotted in figure 24 for several wavenumbers (k_1, k_2). Figue 24(*a*) shows the two-dimensional modes, figure 24(*b*) the mean three-dimensional ($k_1 = 0, k_2 > 0$) and figure 24(*c*) the most important fluctuating three-dimensional disturbances $(1, k_2)$. As described in §2, the Tollmien–Schlichting mode (1,0) and two oblique wave modes $(1, \pm 1)$ are initially excited with their linear eigenfunctions of the amplitudes A_{TS} and A_{3D}. As expected, the Tollmien–Schlichting mode produces significant higher harmonics ($k_1 > 0, 0$) at the beginning due to its finite amplitude of 1.5% of the free-stream velocity. This initial transient is followed by a state of slow steady growth after $t \approx 200$ where the finite-amplitude Tollmien–Schlichting wave grows linearly. The mode (1, 1) shows an initial transient behaviour up to $t \approx 400$. Thereafter it

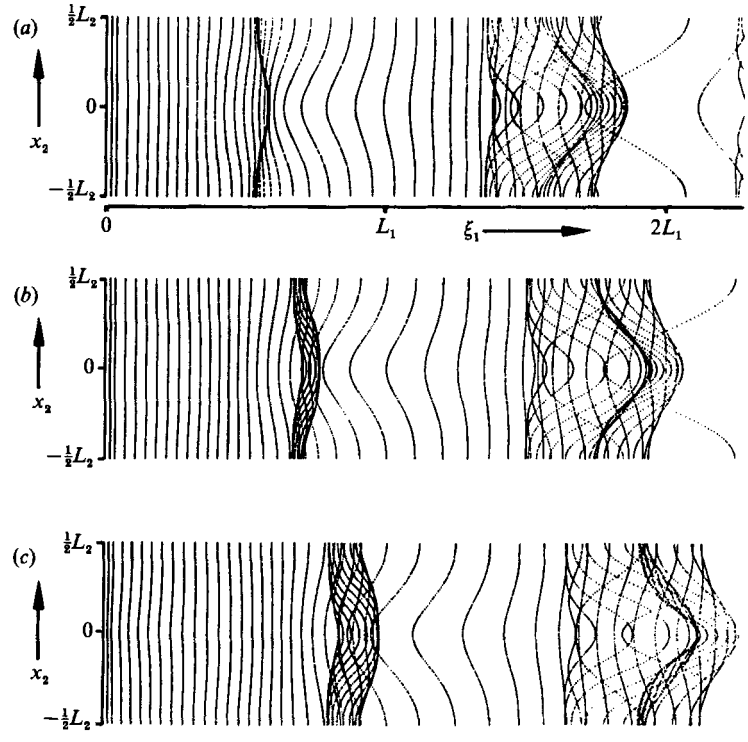

FIGURE 19. Time lines starting from a wire near the critical layer (plan view) at $t = 1100$. (*a*) $\phi = 180°$; (*b*) $\phi = 240°$; (*c*) $\phi = 300°$.

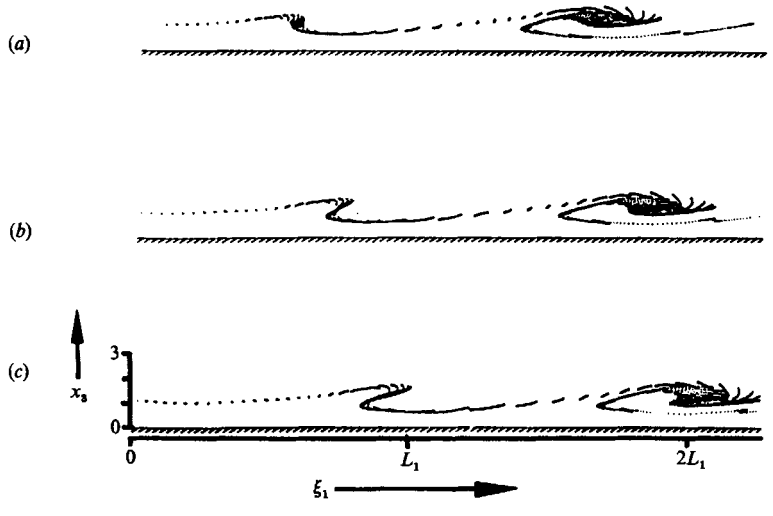

FIGURE 20. Side view of figure 19.

becomes amplified in accordance with the secondary instability. The relatively long initial transient is influenced by the fact that the streamwise and spanwise initial velocity distributions of the $(1, \pm 1)$ mode differed from the exact primary eigenfunction in our runs due to a mistake in the initial velocity computation. However, a comparison run with the exact primary eigenfunction did show the same

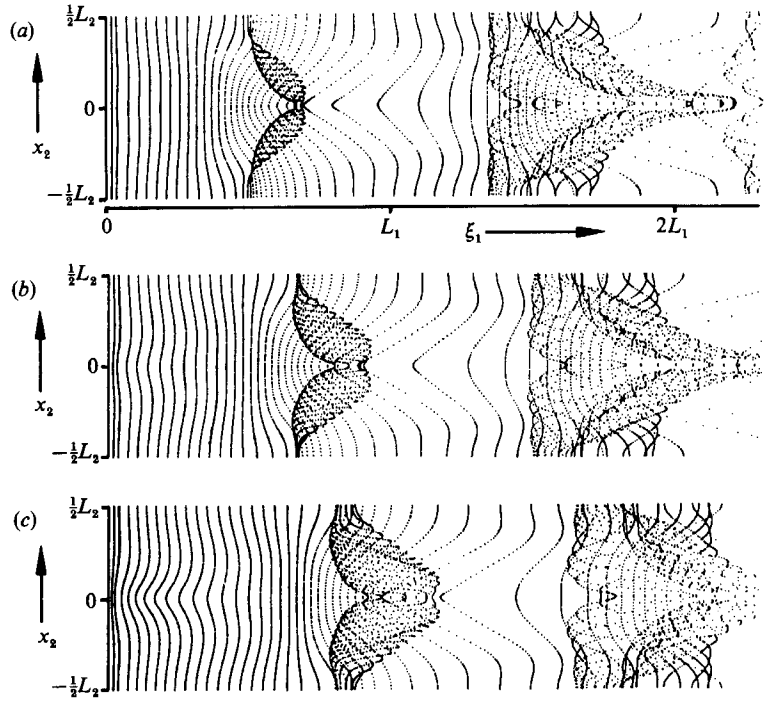

FIGURE 21. Time lines starting from a wire near the critical layer (plan view) at $t = 1200$. (a) $\phi = 180°$; (b) $\phi = 240°$; (c) $\phi = 300°$.

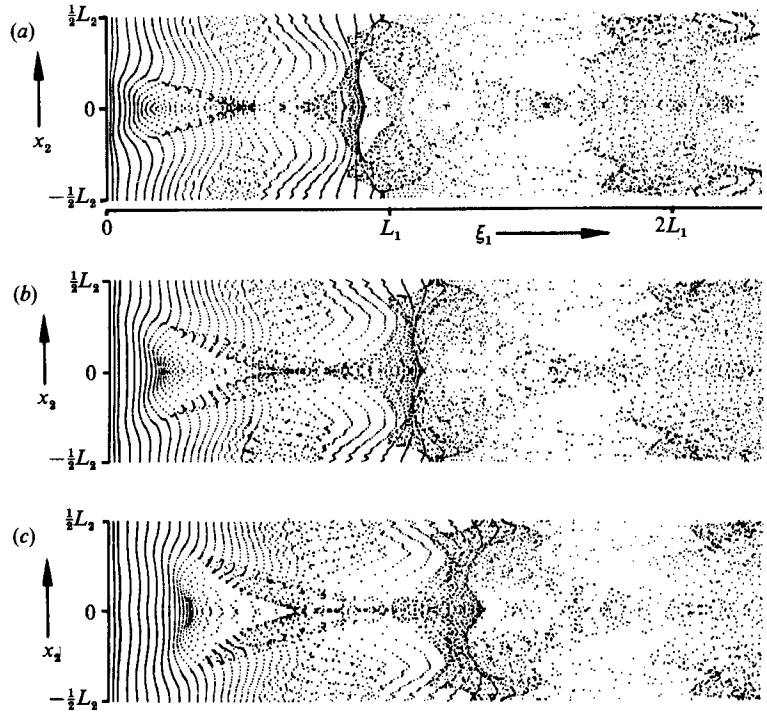

FIGURE 22. Time lines starting from a wire near the critical layer (plan view) at $t = 1260$. (a) $\phi = 180°$; (b) $\phi = 240°$; (c) $\phi = 300°$.

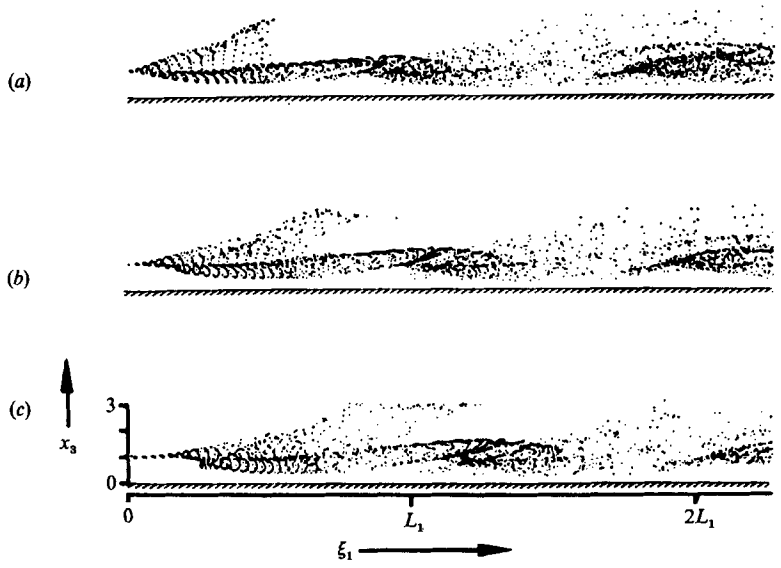

FIGURE 23. Side view of figure 22.

development after the initial transient, during which the $(1, k_2)$ modes assume the shape of the secondary instability eigenfunction.

In the region $t > 400$ two- and three-dimensional disturbances are amplified. We can identify the primary and secondary instabilities in our calculation. When the three-dimensional disturbances grow to finite amplitudes, the process of nonlinear generation of higher harmonic disturbances becomes essential. These disturbances grow relatively slowly in $400 < t < 1000$. Later they grow very fast. The higher spanwise modes grow faster, the larger k_2 is. When the three-dimensional modes reach the amplitudes of the two-dimensional ones, those are also affected at $t > 1200$. The whole process is now governed by strong nonlinear interactions between two- and three-dimensional disturbances.

The observed growth of Fourier modes is completely analogous to that obtained in the Poiseuille flow transition simulations of Kleiser (1982). Although no quantitative comparisons were made, it appears also to be consistent with the experimental results of Kachanov (1987) (cf. his figure 8(*a*); note, however, that the amplitude of the nth harmonic measured at the peak position involves a summation over all spanwise modes (n, k_2)).

The results reported have been obtained with the first option of our forcing terms as described at the beginning of §2, i.e. the basic flow is frozen at the Blasius profile. In order to estimate the influence of the neglected mean flow distortion, a comparison has been made to a second run with the same parameters using the second option of our forcing terms, $f_1 = f_B$. In this comparison run the global mean flow distortion, i.e. the maximum deviation of the Fourier mode (0, 0) from the Blasius profile, was found to be of the order 3×10^{-4} during the initial phase of the simulation. This small magnitude is expected from the Benney–Lin model (see Benney 1964) where the mean flow distortion scales with $O(A_2^2 + A_3^2)$, A_2 and A_3 being the amplitudes of the Tollmien–Schlichting wave and the oblique waves, respectively. After the initial transient the mean flow distortion increases continuously, exceeding the value of 0.01 only shortly before the one-spike stage and attaining the value 0.03 at the end

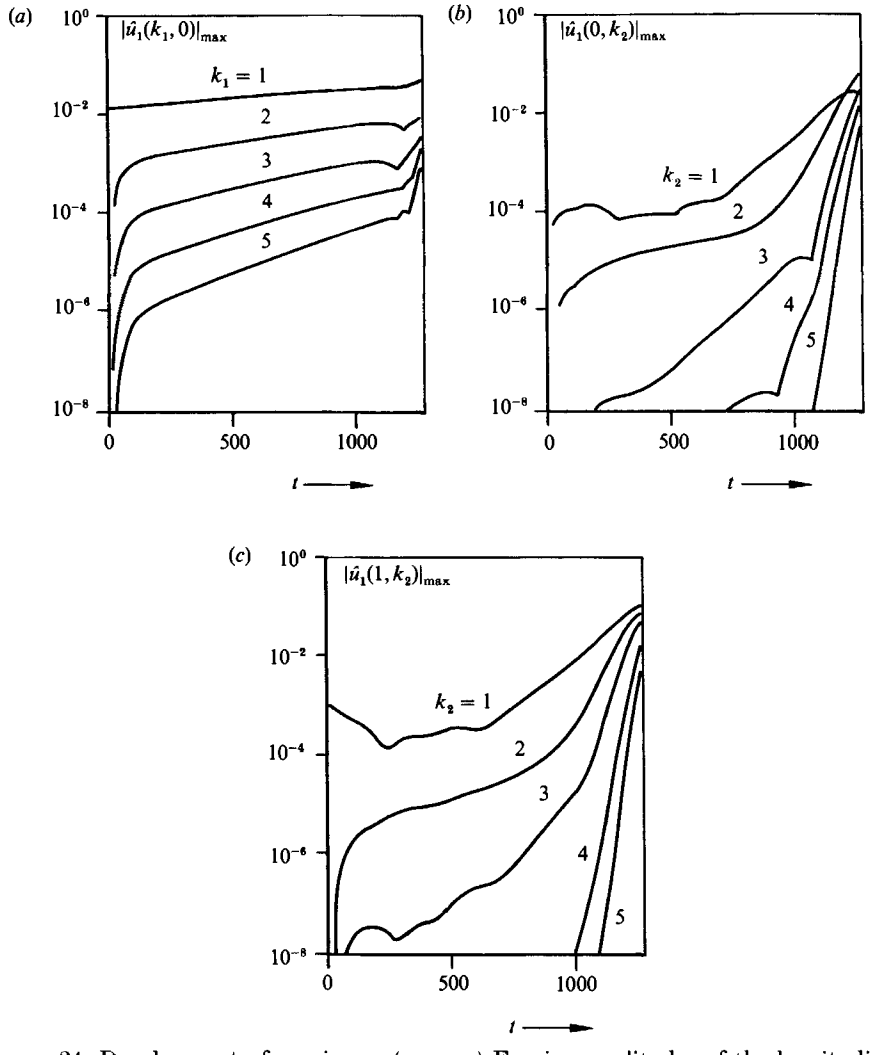

FIGURE 24. Development of maximum (over x_3) Fourier amplitudes of the longitudinal velocity $|\hat{u}_1(k_1, k_2)|_{max}$. (*a*) two-dimensional, (*b*) non-fluctuating three-dimensional, (*c*) fluctuating three-dimensional disturbance modes.

of the simulation. These magnitudes confirm our earlier experience with plane Poiseuille flow transition simulations where the mean flow distortion is always included. The effect on the disturbance modes $(k_1, k_2) \neq (0, 0)$ proved also to be very small. For example, the absolute difference in $u'_{1\max}$ at the peak attained the magnitudes 0.004 at $t = 1000$ and 0.01 at the one-spike stage. However, at later stages the effect of the mean flow distortion will become large and has to be taken into account. Therefore, for future work we recommend including the mean flow distortion by using the forcing term f_B.

We note here that the Tollmien–Schlichting amplification rates obtained from test runs of our numerical code in a wide parameter range are in very good agreement with linear stability theory results computed with an accurate Orr–Sommerfeld solver. The secondary instability has also been investigated by parameter variation. Good quantitative agreement with results of secondary instability calculations has

been found. The secondary instability exhibits a threshold behaviour when the parameter A_{TS} is varied, i.e. the three-dimensional modes are only amplified if the Tollmien–Schlichting amplitude is above a certain threshold. Below this threshold they are always damped. This is in accordance with Orszag & Patera (1983) and Herbert (1983).

5. Subharmonic transition

In this section we describe results of our subharmonic transition simulation. The linear amplification of small three-dimensional subharmonic disturbances has been investigated by Herbert (1983, 1988). We simulate subharmonic transition up to a stage of significant three-dimensionality of the flow structures, and we investigate these structures in detail. The parameters of our subharmonic simulations are $R = 950$, $\alpha_{TS} = 0.153$ and $\alpha_2 = 0.231$. The initial disturbance amplitudes are the same as in the K-type simulations. However, we use here $L_1 = 2L_{TS}$ as noted in the description of (6). This means that now the integration domain is twice as large in the streamwise direction as in a K-type simulation, and that the fundamental wave is the mode $(2, 0)$. Initially the subharmonic three-dimensional disturbance modes $(1, \pm 1)$ are excited. We use the same number of horizontal modes (up to 32^2). Thus the streamwise physical resolution is only half that of the K-type simulations.

5.1. *Symmetries of subharmonic velocity fields*

Before presenting the simulation results we note that our velocity fields $\boldsymbol{u}(\boldsymbol{x}, t)$ show a number of symmetries. First, in the pure subharmonic case we have the *staggered symmetry*

$$u_j\left(\frac{L_1}{2}+x_1, \frac{L_2}{2}+x_2\right) = u_j(x_1, x_2), \tag{19}$$

which due to periodicity is immediately generalized to

$$u_j\left(n\frac{L_1}{2}+x_1, (n+2m)\frac{L_2}{2}+x_2\right) = u_j(x_1, x_2), \tag{20}$$

($j = 1, 2, 3, n, m$ any integers). For the mean and r.m.s. fluctuation quantities therefore

$$\overline{u_j}\left(\frac{L_2}{2}+x_2\right) = \overline{u_j}(x_2), \tag{21}$$

$$u_j'\left(\frac{L_2}{2}+x_2\right) = u_j'(x_2), \tag{22}$$

i.e. periodicity in x_2 with $\frac{1}{2}L_2$ holds. Second, all of our initial disturbances were chosen to be *spanwise-symmetric* according to (7). This initial symmetry is preserved during time integration of the Navier–Stokes equations. From (7) we obtain for the mean components

$$\overline{u_j}\left(n\frac{L_2}{2}+x_2\right) = (-1)^{j+1}\overline{u_j}\left(n\frac{L_2}{2}-x_2\right), \tag{23}$$

and for the r.m.s. fluctuations

$$u_j'\left(n\frac{L_2}{2}+x_2\right) = u_j'\left(n\frac{L_2}{2}-x_2\right), \tag{24}$$

i.e. these quantities are (anti-)symmetric in x_2 about multiples of $\frac{1}{2}L_2$. In our subharmonic simulations both (7) and (19) hold. Thus the velocity field outside the quarter domain $0 \leqslant x_j \leqslant \frac{1}{2}L_j$ is redundant. A code tailored to this case would need only roughly a quarter of the computer time and storage of the general code. For the mean and r.m.s. components we obtain

$$\overline{u_j}\left(n\frac{L_2}{4}+x_2\right) = (-1)^{j+1}\overline{u_j}\left(n\frac{L_2}{4}-x_2\right) \tag{25}$$

$$u_j'\left(n\frac{L_2}{4}+x_2\right) = u_j'\left(n\frac{L_2}{4}-x_2\right). \tag{26}$$

Furthermore, for the velocity components at the spanwise positions $(2n+1)L_2/4$ the relation

$$u_j\left(\frac{L_1}{2}+x_1, \tilde{x}_2\right) = (-1)^{j+1}u_j(x_1, \tilde{x}_2) \quad \left(\tilde{x}_2 = (2n+1)\frac{L_2}{4}\right), \tag{27}$$

holds, i.e. the streamwise and normal components are periodic (and the spanwise component anti-periodic) in x_1 already with $\frac{1}{2}L_1$. All of these symmetries will become apparent in our simulation results.

5.2. *Results and discussion*

First we look at averaged (over two Tollmien–Schlichting wavelengths) quantities. In figure 25 the development of $u'_{1\max}$ at different spanwise positions is shown (for a comparison with the K-type see figure 4). In the subharmonic transition the development starts again with a two-dimensional stage. At $t \approx 400$ a three-dimensional development sets in. The r.m.s. amplitudes at $x_2 = 0$ and $x_2 = \frac{1}{2}L_2$ develop identically. This is in contrast to the K-type development, where these spanwise stations correspond to the peak and valley positions. However, the same fast growth of the fluctuations can be observed once three-dimensionality has occurred. We note that, with the same initial disturbance amplitudes, breakdown occurs earlier in the subharmonic case than in the K-type, figure 4. The u_1' distribution is shown in figure 26 at a beginning three-dimensional stage (figure 26*b*, $t = 560$) and a developed three-dimensional stage (figure 26*c*, $t = 640$). In the subharmonic case a less pronounced peak–valley structure occurs with half the wavelength of the K-type simulation (figure 5). Streamlines of the mean secondary flow are plotted in figure 27. Two pairs of counter-rotating mean longitudinal vortices of the same strength develop in subharmonic transition.

The instantaneous velocity signals shown in figure 28 for $t = 640$ exhibit subharmonics. The signal has identical shape at the spanwise positions $x_2 = 0$ and $x_2 = \frac{1}{2}L_2$ but is shifted by one Tollmien–Schlichting wavelength in the x_1-direction. Thus the spikes appear only every second Tollmien–Schlichting wave at a fixed spanwise position, i.e. in a subharmonic manner. However, the spikes are not as pronounced in this simulation as in the K-type simulation. This may be partly due to the relatively smaller numerical resolution mentioned earlier, although Kachanov (1987) and coworkers report observing no sharp spikes in their subharmonic transition experiments. The phase shift of the velocity signal becomes evident by a plot of the instantaneous shear surface in figure 29 for $t = 640$. The tongue-like structures appear in a staggered pattern, where the two rows of tongues are shifted by half the wavelength L_2 in the x_2-direction according to (20). As a spike signal occurs only at the tip of each tongue the subharmonic behaviour becomes obvious.

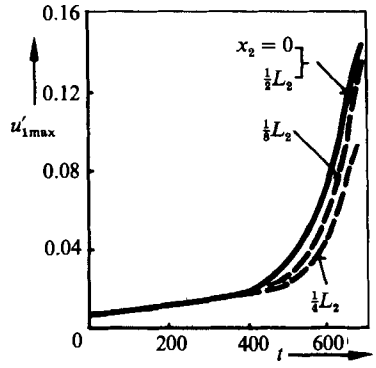

FIGURE 25. Time-development of the maximum longitudinal r.m.s.-fluctuation $u'_{1\max}$ at various spanwise positions in subharmonic transition.

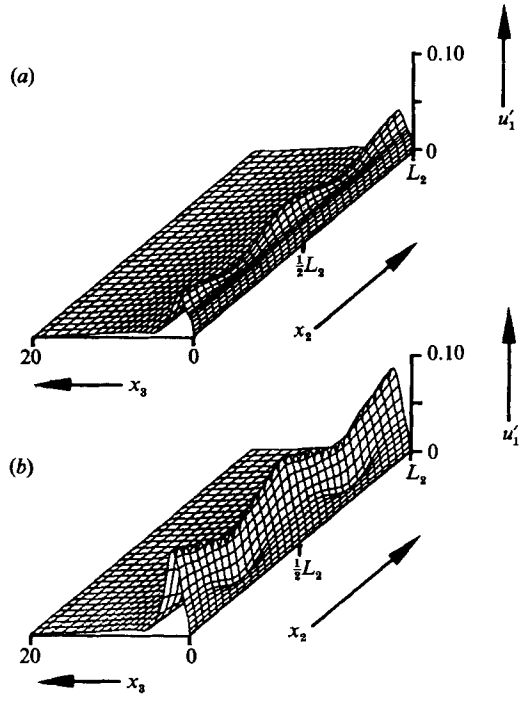

FIGURE 26. Distribution of u'_1 in the subharmonic transition. (*a*) $t = 560$; (*b*) $t = 640$.

Particle visualizations have been computed with the same parameters as for the K-type simulation. The process is now periodic with a period of $2T_{TS}$ instead of T_{TS}. At each Tollmien–Schlichting period T_{TS} A-structures develop downstream of the bubble wire, but the spanwise positions of the structures are shifted by $\frac{1}{2}L_2$ in subsequent cycles. Thus the experimentally observed staggered pattern occurs.

Our results on the subharmonic transition suggest that the formation of three-dimensional instantaneous flow structures is quite similar to the process observed in K-type transition, except for the shift by $\frac{1}{2}L_2$ in the spanwise direction for each cycle. This does not exclude the possibility that a different development may take place if the subharmonic transition process starts with significantly smaller initial disturbance amplitudes, as is the case in some transition experiments.

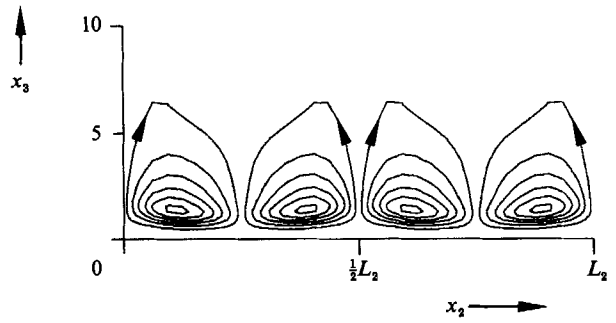

FIGURE 27. Streamlines of the mean secondary flow in subharmonic transition at $t = 640$.

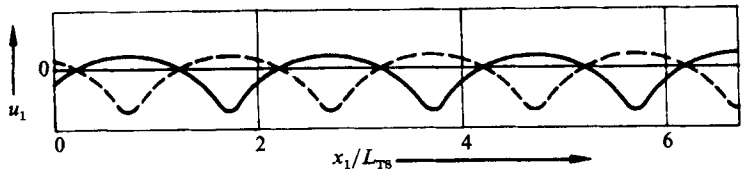

FIGURE 28. Instantaneous velocity signals in subharmonic transition at $t = 640$ at ——, $x_2 = 0$ and ---, $x_2 = \frac{1}{2}L_2$. The vertical scale is arbitrary.

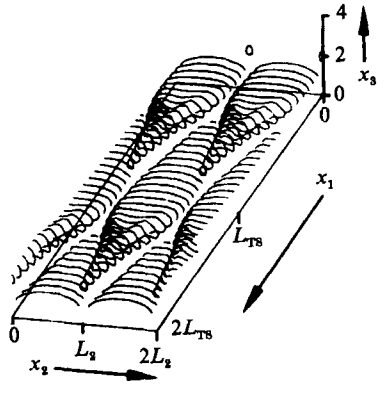

FIGURE 29. Lines of constant instantaneous shear $\partial u_1/\partial x_3 = 0.29$ in subharmonic transition. The region $x_3 < 1.1$ has been suppressed.

6. Transition control by wave superposition

We now apply our simulation model to investigate control of the transition process by superposition of two-dimensional disturbances. The aim of this active control is mainly a transition delay, however, the aspect of transition acceleration will also be considered. In this paper we focus our interest on the processes that occur in the transitional boundary layer after some means of control has been applied. In particular, the reaction of the three-dimensional disturbance parts to the control input will be investigated. The details of the control itself are of less interest here. Also we discuss only the K-type case as qualitatively the same results are obtained in the subharmonic case. As known from the secondary instability theory and from simulations, the growth rate of infinitesimal oblique-wave disturbance modes

depends strongly on the two-dimensional Tollmien–Schlichting wave amplitude. In particular, the three-dimensional disturbances may even be damped if the Tollmien–Schlichting amplitude is below a certain threshold value. We also investigate cases where the oblique-wave disturbances are no longer small and this amplitude dependence is no longer obvious.

6.1. *Control model*

In the experiments referred to in §1 the flow is controlled locally within a small interval in the downstream direction. Accordingly, in our model, control is 'switched on' only within a short time interval $t_A \leqslant t \leqslant t_B$. Outside of this interval the flow develops without any external forcing. While in the experiments the control input is periodic in time, it is periodic x_1 in our simulation. Our control algorithm is designed to influence directly only the fundamental Tollmien–Schlichting mode $(k_1, k_2) = (1, 0)$. An inhomogeneous wall boundary condition $u_{3W}(x_1, t)$ is specified for the normal velocity component,

$$u_{3W}(x_1, t) = u_C(t)\,\mathrm{Re}\{\exp \mathrm{i}(\alpha_{TS} x_1 + \gamma_C)\} \quad (t_A \leqslant t \leqslant t_B), \tag{28}$$

where u_C and γ_C are given below. This boundary condition may be considered as a simple model of a spanwise slot in the wall where fluid is periodically sucked out of or blown into the flow, as in the experiment by Strykowski & Sreenivasan (1985). The mean flux through the wall is zero. It has been verified that this boundary condition, applied to the otherwise undisturbed flow, produces a disturbance which soon develops into a Tollmien–Schlichting wave. The amplitude function $u_C(t)$ and the phase γ_C in (28) are made dependent on quantities 'detected' at the beginning of the control interval, $t = t_A$. Amplitude and phase of the Tollmien–Schlichting mode to be controlled are derived from the normal velocity component u_3. We define the maximum amplitude

$$A_A = \max_{x_3} |\hat{u}_3(1, 0, x_3, t_A)|, \tag{29}$$

and the phase

$$\gamma_A = \arg \hat{u}_3(1, 0, \bar{x}_3, t_A), \tag{30}$$

where $\bar{x}_3 > 5$ is a position just outside the boundary layer, where the phase of the Tollmien–Schlichting wave remains nearly constant. The control amplitude is chosen as the smooth time function

$$u_C(t) = A_A \frac{f}{t_B - t_A}\left(1 - \cos 2\pi \frac{t - t_A}{t_B - t_A}\right), \tag{31}$$

and the phase as

$$\gamma_C = \gamma_A - \Delta\gamma - \gamma_f. \tag{32}$$

Here f and γ_f have been introduced to relate the quantities detected in the flow field to a suitable control input value at the wall. Their values have been optimized to obtain maximum amplitude reduction for a two-dimensional Tollmien–Schlichting wave. For the range of parameters considered the optimum values have been found empirically to be $f = 30$ and $\gamma_f = \frac{1}{4}\pi$. Finally, the imposed phase shift is $\Delta\gamma = \pi$ (antiphased control) for amplitude reduction and $\Delta\gamma = 0$ (in-phase control) for amplification.

The effect of an antiphased control is demonstrated for a typical case in figure 30. A purely two-dimensional Tollmien–Schlichting wave with $R = 950$, $\alpha_{TS} = 0.153$ and an initial amplitude of $A_{TS} = 0.001$ is controlled during $10 \leqslant t \leqslant 60$, corresponding to about half a Tollmien–Schlichting period. At the end of the control interval the amplitudes are reduced by a factor of 3. After control the amplitudes decrease

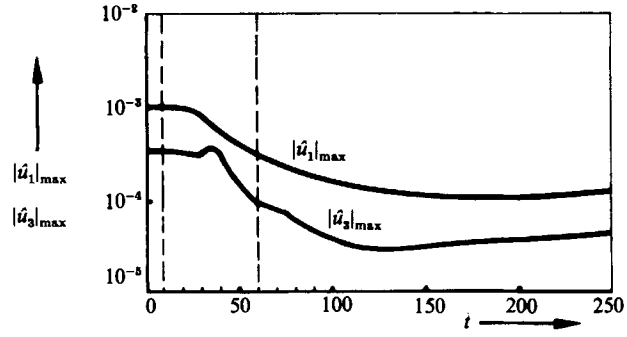

FIGURE 30. Time-development of the maximum Fourier amplitudes of a two-dimensional Tollmien–Schlichting wave with antiphased control in $10 \leqslant t \leqslant 60$.

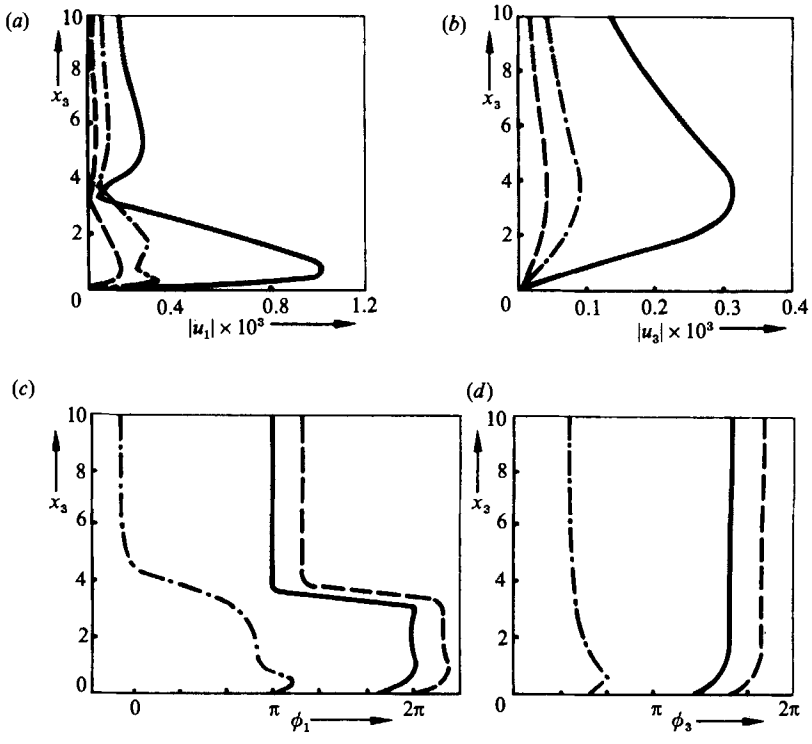

FIGURE 31. Phase and amplitude distributions of controlled Tollmien–Schlichting wave. ——, $t = 10$; –·–, $t = 60$; – – –, $t = 250$.

further, down to a factor of 10 below their initial amplitude. Later the wave is amplified again in accordance with linear stability theory. Figure 31 shows the change of the amplitude and phase distributions which after control gradually relax to the initial Tollmien–Schlichting shape. Thus, the initial disturbance has been reduced in amplitude by an order of magnitude after a delay time of about one oscillation period.

6.2. *Results and discussion*

We now describe our three-dimensional simulations of controlled transition. The parameters and initial conditions are the same as in the uncontrolled K-type

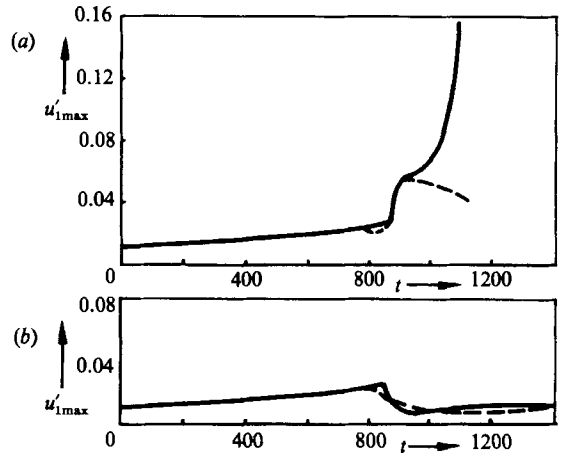

FIGURE 32. Time-development of $u'_{1\max}$ at ——, $x_2 = 0$ and – – –, $x_2 = \frac{1}{2}L_2$ with control in $850 \leqslant t \leqslant 900$. (*a*) in-phase; (*b*) antiphased control.

simulation of §4 to which the results will be compared. First we consider results of two simulations with control during $850 \leqslant t \leqslant 900$, one with in-phase and the other with antiphased control. The control interval is placed at the beginning of the three-dimensional development. The behaviour of the maximum fluctuations at the peak and valley positions is shown in figure 32 (for a comparison with the uncontrolled case see figure 4). With in-phase control the fluctuations at both spanwise positions grow rapidly within the control interval. Thereafter a pronounced three-dimensional development sets in, as indicated by the splitting of the two curves. At the peak position $x_2 = 0$ the fluctuations grow rapidly and reach typical spike stage values of 0.15 at an earlier time (roughly at $t = 1100$) than in the uncontrolled case (at $t = 1260$). Thus transition has been accelerated by in-phase control. The antiphased control reduces the fluctuations and no further growth occurs until $t = 1400$. Transition has been delayed by two-dimensional antiphased control. This case is discussed in more detail below.

Having demonstrated that transition can be delayed in our simulation, we investigate now the limitations of the two-dimensional antiphased control. In particular, we ask what magnitude the three-dimensional disturbances may have for a two-dimensional control still to be successful, and how far transition can be delayed. The results of three simulations differing only in the time position of the control interval are compared:

case I: control in $850 \leqslant t \leqslant 900$,

case II: control in $1000 \leqslant t \leqslant 1050$,

case III: control in $1150 \leqslant t \leqslant 1200$.

Case I is the same as shown in figure 32 (*b*). The maximum fluctuations for the three cases are shown in figure 33 and compared with the uncontrolled simulation. In case I transition is controlled in an early stage, where the flow is governed by the two-dimensional Tollmien–Schlichting wave. After its amplitude has been reduced by the control, the transition process proceeds in the same manner as uncontrolled transition. This was checked by comparing the flow structures such as $u'_1(x_2, x_3)$, the mean longitudinal vortex system, and the constant-shear surface with uncontrolled transition (Laurien 1986), which turned out to be the same. In case III the control is applied at a developed three-dimensional stage and has only a very weak effect on

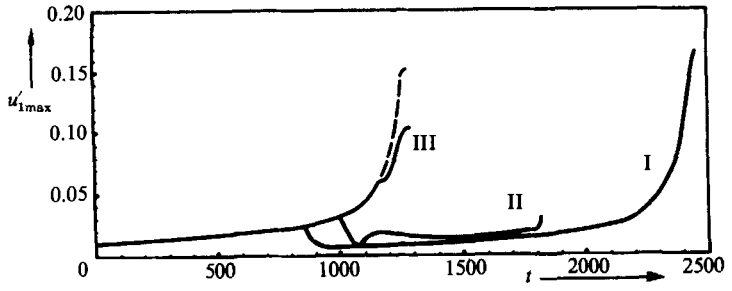

FIGURE 33. Time-development of $u'_{1\max}$ at $x_2 = 0$ of ---, the non-controlled case and ——, three controlled cases: I, control in $850 \leqslant t \leqslant 900$; II, control in $1000 \leqslant t \leqslant 1050$; III, control in $1150 \leqslant t \leqslant 1200$.

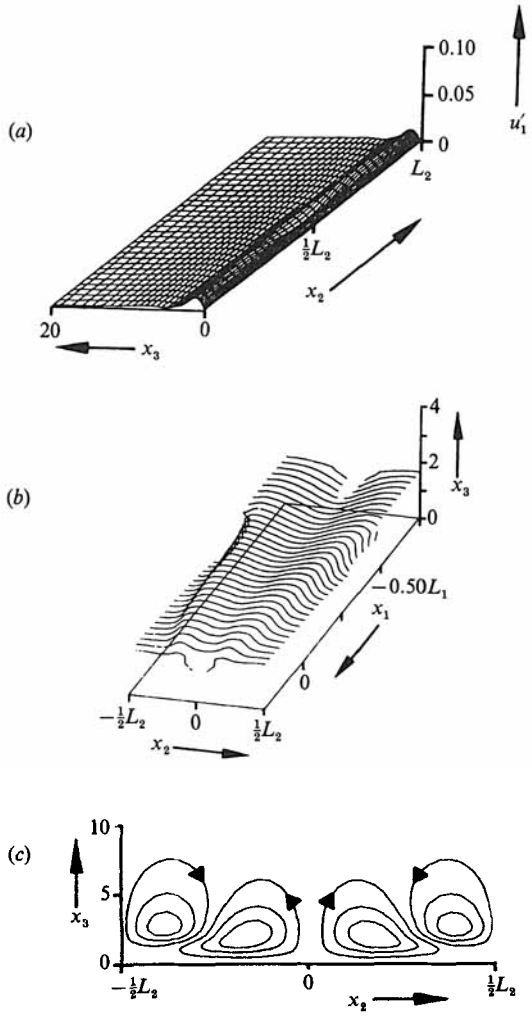

FIGURE 34. Flow structures in the controlled case II at $t = 1400$. (*a*) r.m.s. fluctuations; (*b*) lines of constant shear $\partial u_1/\partial x_3 = 0.29$; (*c*) streamlines of mean secondary flow.

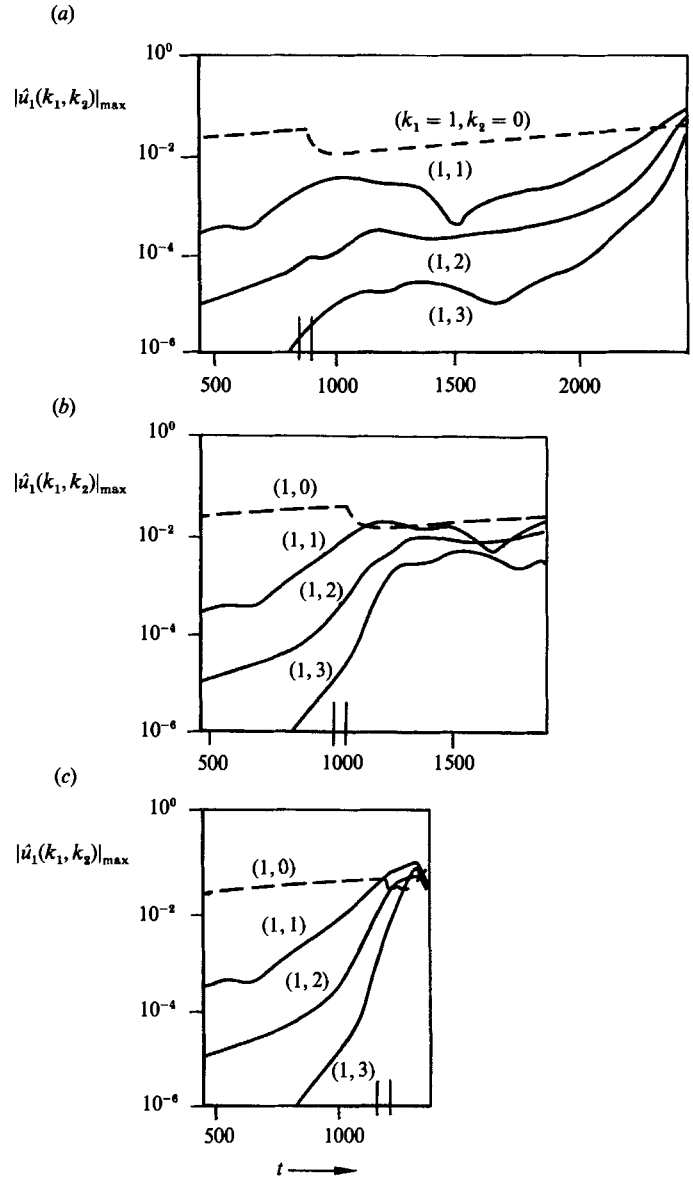

FIGURE 35. Development of the maximum Fourier amplitudes – – –, of the Tollmien–Schlichting wave and ——, of the most important fluctuating disturbances. (*a*) case I; (*b*) case II; (*c*) case III.

the fluctuations. The flow structures in the spike stage are almost the same as in uncontrolled transition.

However, in case II the structures develop differently. Figure 34 shows the structures obtained in case II at $t = 1400$, i.e. some time after control. The r.m.s. fluctuations are small and show nearly no spanwise variation (figure 34*a*). The instantaneous shear is shown in figure 34(*b*). There is only a weak streamwise waviness, but a strong variation in the spanwise direction. This means that the fluctuations, i.e. the variations in x_1, are small (see also figure 33 at $t = 1400$). However, the mean flow is markedly three-dimensional. The corresponding mean

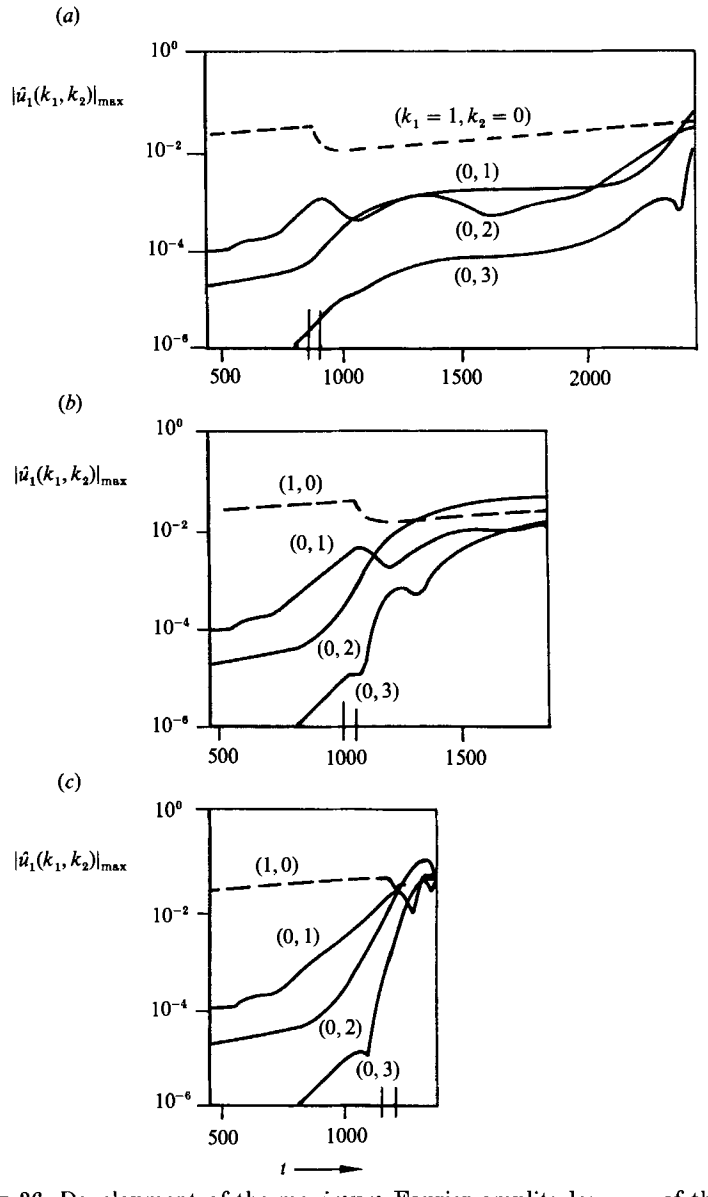

FIGURE 36. Development of the maximum Fourier amplitudes ---, of the Tollmien–Schlichting wave and ——, of the most important non-fluctuating disturbances. (*a*) case I; (*b*) case II; (*c*) case III.

longitudinal vortex system is shown in figure 34(*c*). It is similar to that observed in uncontrolled transition at a developed three-dimensional stage $t = 1220$ (see figure 6). We did not follow the development of this simulation further than $t = 1800$ as the structures could not be resolved any more by the numerical discretization used in this case.

Fourier amplitudes of the most important three-dimensional fluctuating and non-fluctuating disturbance modes are examined for cases I–III in figures 35 and 36. In addition the Tollmien–Schlichting mode (1, 0) is shown for comparison. In case I the three-dimensional disturbances are still much smaller than the two-dimensional ones

at the beginning of control. As expected, the three-dimensional growth is reduced after control has been applied. Some time later the fluctuating three-dimensional mode is even damped. However, this damping occurs only after a delay time of roughly 200 time units after the end of control. As the Tollmien–Schlichting wave grows again later all disturbances are finally amplified. In case II the three-dimensional disturbances are still smaller than the two-dimensional ones at the beginning of control although they are by then larger than in case I. After control the three-dimensional amplification is first reduced and then stopped. The (1, 1) mode is even damped after a delay time of about 300. We see that the effect of the control on the fluctuating disturbances is much more pronounced than on the non-fluctuating disturbances. The latter grow even if the (1, 1) mode is already damped. This is consistent with our observations in figure 34 where the fluctuations are reduced but the mean three-dimensionality is still pronounced. In case III, two- and three-dimensional disturbances are of the same order of magnitude at the beginning of control. There is nearly no visible effect of the control on the three-dimensional disturbances.

Our simulations with antiphased disturbances confirm the expected result that a two-dimensional active control is more successful if it is applied in the early stages of the transition process, where the three-dimensional disturbances are still smaller than the two-dimensional ones. While the fluctuations can be reduced successfully, the mean longitudinal vortex system, once produced in the transition process, remains in the flow even after transition has been delayed successfully. Three-dimensional disturbances are affected by control only after a time delay once they have grown to a finite amplitude, as observed in cases I and II. We observe that the effect on the non-fluctuating three-dimensional disturbances is weaker than on the fluctuating disturbances, i.e. the time delay is larger. A two-dimensional control is not successful if it is applied in a developed three-dimensional stage where the fluctuations exceed the order of 5%, say. Here two- and three-dimensional disturbances are of the same order of magnitude and control cannot be successful, as the higher harmonic disturbances already grow very rapidly and lead to breakdown before control could have an effect. The nonlinear dynamical interaction of two-dimensional and fluctuating and non-fluctuating three-dimensional disturbances are essential in controlled transition.

7. Conclusions

We have simulated numerically the laminar–turbulent transition process and its control by wave superposition using a simple model of the Blasius boundary layer. In this model the basic flow is assumed to be parallel and constant and the Reynolds number is kept fixed. Streamwise and spanwise periodic disturbances developing in time are considered. Both the classical Klebanoff-type and the subharmonic type of transition are simulated. The simulations are based on the three-dimensional time-dependent Navier–Stokes equations. A spectral method with Fourier expansions in the horizontal directions and Chebyshev matrix collocation in the normal direction is used. The latter becomes efficient through the use of a matrix diagonalization technique. The pressure is calculated with the aid of an influence matrix method. We simulate laminar–turbulent transition up to the spike stage using a numerical discretization with up to $32 \times 32 \times 48$ grid points.

The simulation results are compared with hot-wire measurements and flow visualizations by other authors. We find that the stages of timewise development in

our simulations can be related to corresponding stages of the downstream development in the experiments. Averaged quantities, such as r.m.s. fluctuations and mean secondary flow, and instantaneous quantities have been compared in detail for the case of K-type transition. At corresponding stages our results agree surprisingly well with the experiments. Our visualizations with numerically integrated particles give results very similar to experimental hydrogen-bubble visualizations for both the K-type and the subharmonic type of transition.

We can identify the basic mechanisms of the subsequent stages of the boundary-layer transition process in our simulations. First the Blasius profile becomes unstable with respect to two-dimensional Tollmien–Schlichting waves. This is referred to as the primary instability. Once these waves reach a certain threshold amplitude, initially small three-dimensional disturbances become amplified. This step can well be described by a linear secondary instability theory (Orszag & Patera 1983; Herbert 1983, 1988). Depending on the parameters and initial conditions either the classical K-type structures or subharmonic structures appear in the next stages of development. The formation of three-dimensional structures in the flow is due to nonlinear interactions of finite-amplitude two- and three-dimensional amplified disturbances. The instantaneous velocity field can be described using the picture of a three-dimensional vortex loop, the so-called 'horseshoe vortex', which is travelling downstream with approximately the Tollmien–Schlichting wave speed. On its way downstream the horseshoe vortex is stretched and tilted (Orszag & Patera 1983). Behind its forward tip the vortex induces a strong instantaneous upward motion, transporting slow fluid away from the wall. Thus a region of high shear $\partial u_1/\partial x_3$ is formed. The instantaneous spikes in the velocity signals are caused by the local strong upward motion. As the vortex loop contains significant streamwise vorticity the strengthening of the longitudinal vortices can be ascribed to the stretching of the vortex loop.

Our results illuminate the relation of the instantaneous flow field to the structures observed in flow visualizations. The well-known folding of the particle sheet near the critical layer of a Tollmien–Schlichting wave becomes more and more three-dimensional in the velocity field induced by the horseshoe vortex. In a three-dimensional stage the folding pattern appears as the so-called Λ-structure. We note that our interpretation of the instantaneous velocity and vorticity field is consistent with the explanation given by Williams *et al.* (1984) for the corresponding experimentally obtained data in the case of K-type transition.

We have applied our simulation model to investigate active control of boundary-layer transition by superposition of periodic disturbances. Two-dimensional control waves are introduced locally within a small time interval by periodic wall suction and blowing. A two-dimensional control can be successful because the amplification of small three-dimensional disturbances strongly depends on the amplitude of the two-dimensional Tollmien–Schlichting wave. We find that the transition process can be controlled even in the presence of three-dimensional disturbances of finite (but not too large) amplitude. However, the disturbances are affected by the control input only with some time delay. Out-of-phase control delays transition if it is applied in an early stage. In later strongly three-dimensional stages, two-dimensional control is no longer successful. Even if transition has been successfully delayed, mean longitudinal vortices remain in the flow.

We conclude that the transition process in a Blasius boundary layer up to the one-spike stage is well described by our model. Numerical simulation represents a powerful tool for investigating transition which, in particular, permits easy access to the data of all three-dimensional flow quantities at any stage of development.

We thank F. Meyer for performing some additional calculations and two referees for suggesting improvements to the text of our manuscript.

REFERENCES

ARNAL, D. 1984 Description and prediction of transition in two-dimensional incompressible flow. In *Special Course on Stability and Transition of Laminar Flow* (ed. R. Michel). *AGARD-R*-709, 2.1–2.47.

BENNEY, D. J. 1964 Finite amplitude effects in an unstable laminar boundary layer. *Phys. Fluids* **7**, 319–326.

CANUTO, C., HUSSAINI, M. Y., QUARTERONI, A. & ZANG, T. A. 1987 *Spectral Methods in Fluid Dynamics*. Springer.

CRAIK, A. D. D. 1971 Non-linear resonant instability in boundary layers. *J. Fluid Mech.* **50**, 393–413.

EPPLER, R. & FASEL, H. 1980 Laminar-turbulent transition. *Proc. IUTAM Symposium, Stuttgart, 1979*. Springer.

FASEL, H. F., RIST, U. & KONZELMANN, U. 1987 Numerical investigation of the three-dimensional development in boundary layer transition. *AIAA Paper* 87-1203.

GASTER, M. 1962 A note on the relation between temporally-increasing and spatially-increasing disturbances in hydrodynamic stability. *J. Fluid Mech.* **14**, 222–224.

GOTTLIEB, D., HUSSAINI, M. Y. & ORSZAG, S. A. 1984 Theory and applications of spectral methods. In *Spectral Methods for Partial Differential Equations* (ed. R. G. Voigt, D. Gottlieb & M. Y. Hussaini), pp. 1–54. SIAM, Philadelphia.

HAMA, F. R. 1962 Streaklines in perturbed shear flow. *Phys. Fluids* **5**, 644–650.

HAMA, F. R. & NUTANT, J. 1963 Detailed flow-field observations in the transition process in a thick boundary layer. *Proc. 1963 Heat Transfer and Fluid Mech. Institute* 77–93.

HAMA, F. R., RIST, U., KONZELMANN, U., LAURIEN, E. & MEYER, F. 1987 Vorticity field structure associated with the 3D Tollmien–Schlichting waves. *Sādhanā, Academy Proc. Engng Sci., Indian Acad. Sci.* **10**, 321–347.

HERBERT, TH. 1983 Subharmonic three-dimensional disturbances in unstable plane shear flows. *AIAA Paper* 83-1759.

HERBERT, TH. 1988 Secondary instability of boundary layers. *Ann. Rev. Fluid Mech.* **20**, 487–526.

HUERRE, P. 1987 On the Landau constant in mixing layers. *Proc. R. Soc. Lond.* A **409**, 369–381.

KACHANOV, YU. S. 1987 On the resonant nature of the breakdown of a laminar boundary layer. *J. Fluid Mech.* **184**, 43–47.

KACHANOV, YU. S. & LEVCHENKO, V. YA. 1984 The resonant interaction of disturbances at laminar-turbulent transition in a boundary layer. *J. Fluid Mech.* **138**, 209–247.

KLEBANOFF, P. S., TIDSTROM, K. D. & SARGENT, L.M. 1962 The three-dimensional nature of boundary-layer instability. *J. Fluid Mech.* **12**, 1–34.

KLEISER, L. 1982 *Spectral Simulations of Laminar-Turbulent Transition in Plane Poiseuille Flow and Comparison with Experiments*. Lecture Notes in Physics, vol. 170, pp. 280–285. Springer.

KLEISER, L. & LAURIEN, E. 1985*a* Three-dimensional numerical simulation of laminar-turbulent transition and its control by periodic disturbances. In *Laminar-Turbulent Transition. Proc. 2nd IUTAM Symp. Novosibirsk, 1984* (ed. V. V. Kozlov), pp. 29–37. Springer.

KLEISER, L. & LAURIEN, E. 1985*b* Numerical investigation of interactive transition control. *AIAA Paper* 85-0566.

KLEISER, L. & SCHUMANN, U. 1980 Treatment of incompressibility and boundary conditions in 3-D numerical spectral simulations of plane channel flows. *Proc. 3rd GAMM Conference on Numerical Methods in Fluid Mechanics* (ed. E. H. Hirschel), pp. 165–173. Vieweg, Braunschweig.

KLEISER, L. & SCHUMANN, U. 1984 Spectral simulations of the laminar-turbulent transition process in plane Poiseuille flow. In *Spectral Methods for Partial Differential Equations* (ed. R. G. Voigt, D. Gottlieb & M. Y. Hussaini), pp. 141–163. SIAM, Philadelphia.

KOVASZNAY, L. S. G., KOMODA, H. & VASUDEVA, B. R. 1962 Detailed flow field in transition. *Proc. 1962 Heat Transfer and Fluid Mech. Institute* 1–26.

KOZLOV, V. V. 1985 *Laminar-Turbulent Transition. Proc. 2nd IUTAM Symp. Novosibirsk, 1984.* Springer.

LAURIEN, E. 1986 Numerische Simulation zur aktiven Beeinflussung des laminar – turbulenten Übergangs in der Plattengrenzschichtströmung. Dissertation, Universität Karlsruhe, Rep. DFVLR-FB 86-05. English translation in ESA-TT 995 (1987).

LAURIEN, E. & KLEISER, L. 1986 Numerical simulation of transition control in boundary layers. In *Proc. Sixth Gamm Conference on Numerical Methods in Fluid Mechanics* (ed. D. Rues & W. Kordulla), pp. 225–232. Vieweg, Braunschweig/Wiesbaden.

LIEPMANN, H. W., BROWN, G. L. & NOSENCHUCK, D. M. 1982 Control of laminar-instability waves using a new technique. *J. Fluid Mech.* **118**, 187–200.

LIEPMANN, H. W. & NOSENCHUCK, D. M. 1982 Active control of laminar-turbulent transition. *J. Fluid Mech.* **118**, 201–204.

METCALFE, R. W., RUTLAND, C. J., DUNCAN, J. H. & RILEY, J. J. 1986 Numerical simulations of active stabilization of laminar boundary layers. *AIAA J.* **24**, 1494–1501.

MILINAZZO, F. A. & SAFFMAN, P. G. 1985 Finite-amplitude steady waves in plane viscous shear flows. *J. Fluid Mech.* **160**, 281–295.

MILLING, R. W. 1981 Tollmien–Schlichting wave cancellation. *Phys. Fluids* **24**, 979–981.

ORSZAG, S. A. & KELLS, L. C. 1980 Transition to turbulence in plane Poiseuille flow and plane Couette flow. *J. Fluid Mech.* **96**, 159–206.

ORSZAG, S. A. & PATERA, A. T. 1981 Subcritical transition to turbulence in plane shear flows. In *Transition and Turbulence* (ed. R. E. Meyer), pp. 127–146. Academic.

ORSZAG, S. A. & PATERA, A. T. 1983 Secondary instability of wall-bounded shear flows. *J. Fluid Mech.* **128**, 347–385.

PATERA, A. T. & ORSZAG, S. A. 1981 Finite-amplitude stability of axisymmetric pipe flow. *J. Fluid Mech.* **112**, 467–474.

SARIC, W. S., KOZLOV, V. V. & LEVCHENKO, V. YA. 1984 Forced and unforced subharmonic resonance in boundary-layer transition. *AIAA Paper* 84-0007.

SPALART, P. R. 1984 A spectral method for external viscous flows. *Contemp. Math.* **28**, 315–335.

SPALART, P. R. 1986 Numerical simulation of boundary layers. Part 1. Weak formulation and numerical method. *NASA Tech. Mem.* 88222.

SPALART, P. R. & YANG, K.-S. 1987 Numerical study of ribbon-induced transition in Blasius flow. *J. Fluid Mech.* **178**, 345–365.

STRYKOWSKI, P. J. & SREENIVASAN, K. R. 1985 The control of transitional flows. *AIAA Paper* 85-0559.

TANI, J. 1969 Boundary-layer transition. *Ann. Rev. Fluid Mech.* **1**, 169–196.

THOMAS, A. S. W. 1983 The control of boundary-layer transition using a wave-superposition principle. *J. Fluid Mech.* **137**, 233–250.

WILLIAMS, D. R. 1985 Vortical structures in the breakdown stage of transition. *Proc. ICASE/NASA Workshop on Stability of Time Dependent and Spatially Varying Flows.* Springer.

WILLIAMS, D. R., FASEL, H. & HAMA, F. R. 1984 Experimental determination of the three-dimensional vorticity field in the boundary-layer transition process. *J. Fluid Mech.* **149**, 179–203.

WORTMANN, F. X. 1977 The incompressible fluid motion downstream of two-dimensional Tollmien–Schlichting waves. *AGARD-CP*-224, 12.1–12.8.

WRAY, A. & HUSSAINI, M. Y. 1984 Numerical experiments in boundary-layer stability. *Proc. R. Soc. Lond.* A **392**, 373–389.

ZANG, T. A. & HUSSAINI, M. Y. 1985*a* Numerical experiments on subcritical transition mechanisms. *AIAA Paper* 85-0296.

ZANG, T. A. & HUSSAINI, M. Y. 1985*b* Numerical experiments on the stability of controlled shear flows. *AIAA Paper* 85-1698.

ZANG, T. A. & HUSSAINI, M. Y. 1987 Numerical simulation of nonlinear interactions in channel and boundary-layer transition. In *Nonlinear Wave Interactions in Fluids* (ed. R. W. Miksad, T. R. Akylas & T. Herbert), ASME, AMD-vol. 87, 131–145.